Department of Physics and Astronomy
Heidelberg University

Bachelor Thesis in Physics
submitted by

Michael Uwe Gotzmann

born in Singen (Hohentwiel) (Germany)

2024

Low Temperature Ion Diffusion Erbium-Doping in Thin-film Lithium Niobate

This Bachelor Thesis has been carried out by Michael Uwe Gotzmann at the Kirchhoff-Institut für Physik of the Ruprecht-Karls-University of Heidelberg
under the supervision of
Prof. Dr. Wolfram Pernice

Abstract

In light of the increasing importance of telecommunications and its applications on platforms such as lithium niobate, optical power loss from active components on photonic chips present a growing challenge. This study investigates compensating these losses through stimulated emission of the $^4I_{13/2} \rightarrow ^4I_{15/2}$ transition of the lanthanoid erbium, introduced into the lithium niobate coating of the waveguide chips via low temperature ion diffusion. Continuous quality control using scanning electron microscopy (SEM) and energy-dispersive X-ray spectroscopy (EDS) identified optimal doping parameters to be a solution of 27 g potassium-salt and 0.4 g erbium-salt, a diffusion duration of 4 hours at 465°C, and annealing at 200°C, 300°C, and 400°C for 4, 4, and 23 hours, respectively. The most effective cleaning of the chip surfaces, achieving 100% potassium and over 80% erbium impurity removal, was accomplished using distilled water, citric acid, and sodium thiosulfate. Measurement series to characterize both stimulated and spontaneous emission were conducted using fiber-coupled and free-space setups. The developed method, combined with additional surface cleaning and local masking, e.g., with SiO_2, enables precise local doping of photonic structures.

Zusammenfassung

Angesichts der zunehmenden Bedeutung der Telekommunikation und ihrer Anwendungen auf Plattformen wie Lithiumniobat stellen optische Leistungsverluste von aktiven Komponenten auf photonischen Chips eine wachsende Herausforderung dar. Diese Arbeit untersucht die Kompensation dieser Verluste durch stimulierte Emission des Übergangs $^4I_{13/2} \rightarrow ^4I_{15/2}$ des Lanthanoids Erbium, das mittels Niedrigtemperatur-Ionendiffusion in die Lithiumniobatbeschichtung der verwendeten Wellenleiterchips eingebracht wird. Durch kontinuierliche Qualitätskontrollen mittels Rasterelektronenmikroskopie (SEM) und energiedispersiver Röntgenspektroskopie (EDS) ergaben sich als optimale Doping-Parameter eine Lösung aus 27 g Kalium und 0,4 g Erbium, eine Diffusionsdauer von 4 Stunden bei 465°C sowie ein Tempern bei 200°C, 300°C und 400°C für jeweils 4, 4 und 23 Stunden. Die effektivste Reinigung der Chipoberflächen, bei der 100% der Kalium- und über 80% der Erbiumverunreinigungen entfernt wurden, erfolgte unter Verwendung von destilliertem Wasser, Zitronensäure und Natrium Thiosulfat. Messreihen zur Charakterisierung der stimulierten und spontanen Emission wurden sowohl mit fasergekoppelten als auch Freistrahl-Versuchsaufbauten durchgeführt. Die entwickelte Methode, kombiniert mit einer zusätzlichen Oberflächenreinigung und lokalem Maskieren, z.B. mit SiO_2, ermöglicht ein präzises lokales Doping photonischer Strukturen.

Contents

1 Introduction

Telecommunication has become the backbone of modern society, facilitating the exchange of vast amounts of information across the globe. Every day, approximately 5 exabytes of data are transmitted, enabling everything from simple text messages to complex financial transactions [1]. While it may seem that the majority of this data is transferred wirelessly, in reality, over 99% of intercontinental data traffic is carried through undersea and land-based optical fiber cables [2]. These extensive networks form the critical infrastructure that supports our digital world.

However, these vast networks of optical fibers face significant challenges due to optical power losses over long distances. These losses, primarily caused by scattering, absorption, and other imperfections in the fiber material, can severely degrade signal quality [3]. To mitigate these losses, Erbium-Doped Fiber Amplifiers (EDFAs) are employed. EDFAs use the element erbium to boost signal strength through a process known as stimulated emission of radiation, allowing the signals to travel longer distances without significant loss of quality [4]. While this technique is highly effective, it represents just one aspect of the broader landscape of photonic signal processing.
Because telecommunication does not only rely on large-scale infrastructure like optical cables but increasingly also on small-scale integrated photonics. A prominent material in this field is lithium niobate ($LiNbO_3$), which has emerged as a superior platform for integrated photonics. Lithium niobate is renowned for its excellent electro-optical, acousto-optical, and nonlinear optical properties, making it highly suitable for various signal processing applications, including modulators, switches, and frequency converters [5]. However, despite these advantages, integrating active components like electro-optic modulators (EOMs), phase shifters, and wavelength converters on a lithium niobate platform can lead to significant signal losses [6], [7] and [8]. These losses are detrimental to the overall performance and efficiency of photonic circuits.

To address these challenges, one promising approach also involves erbium doping comparable to the EDFA, because erbium-doped lithium niobate can also serve as an effective medium for optical amplification, compensating for signal losses within the integrated photonic circuits [9]. While commercially available erbium-doped lithium niobate wafers [10] are produced using the Czochralski method [11], [12], these wafers present several challenges. The primary issue is that doping the entire wafer can degrade the performance of active components. This degradation necessitates a more localized doping

approach. Localized doping is not only more material- and cost-efficient, but it also allows for targeted enhancement of specific regions, thereby improving performance without affecting the entire chip.

The focus of this Bachelor thesis is to develop an optimized recipe for local erbium doping of lithium niobate using Low Temperature Ion Diffusion (LTID). LTID offers several advantages over high-temperature methods, including reduced thermal stress and fewer defects in the material [13]. By concentrating the doping process in specific areas, we can enhance the functionality of photonic devices while maintaining the integrity of undoped regions.

This thesis will explore the theoretical foundations of thin-film lithium niobate and erbium doping, along with the operational principles of erbium-doped amplifiers. The methodologies section will detail the experimental setup for erbium doping, the fabrication of waveguides, and the use of scanning electron microscopy (SEM) combined with energy-dispersive X-ray spectroscopy (EDS). In the results section, the optimization of the erbium-doping process will be presented, along with measurements conducted using fiber-coupled transmission and reflection setups, as well as free-space setup results. The thesis will conclude with a comprehensive discussion and future outlook, aiming to contribute valuable insights into the local doping of lithium niobate for integrated photonic applications.

2 Theoretical Background

The following section will introduce the theoretical fundamentals, with a particular focus on thin-film lithium niobate, erbium doping, and the operational principle of erbium-doped amplifiers in the context of this Bachelor's thesis.

2.1 Thin-Film Lithium-Niobate

Thin-film nithium niobate (TFLN) is of great significance in the field of integrated and guided-wave optics. The ferroelectric crystal is not a naturally occurring substance; it was first produced artificially in 1965 by Ballmann [14] using the Czochralski technique [15]. The inaugural integrated waveguide was subsequently manufactured in 1974 by Schmidt and Kaminow via a metal-diffusion process. This resulted in the formation of low-loss TE and TM mode optical waveguides [14]. The ferroelectric nature of the material was first identified in 1949 [16].

As illustrated in Figure 1, the crystal structure of lithium niobate, $LiNbO_3$ (LN) designated to the 3m point group. The value of "3" indicates the rotation symmetry axis, which is tripled (120°) and situated along the main Z-axis (also known as C-axis). The "m" indicates that there are three layers orthogonal to the Z-axis, with each layer including the Z-axis and cutting the whole lattice in two halves [17]. With regard to LN, this signifies that the lithium (Li) -ions (Li^+ and niobium (Nb) ions (Nb^{5+}) are positioned within octahedral voids created by oxygen (O) -ions (O^{2-}), and moreover, the O-ions form a distorted hexagonal arrangement. This arrangement gives rise to the distinctive electrical, optical and acoustic properties of LN [18], which will be discussed in more detail in the following section.

Figure 1 illustrates the relative positions of Li and Nb, including the O octahedra. Along the Z-axis, the octahedra are filled in the sequence Li, Nb, vacancy, Li, Nb, vacancy, and so forth [19].

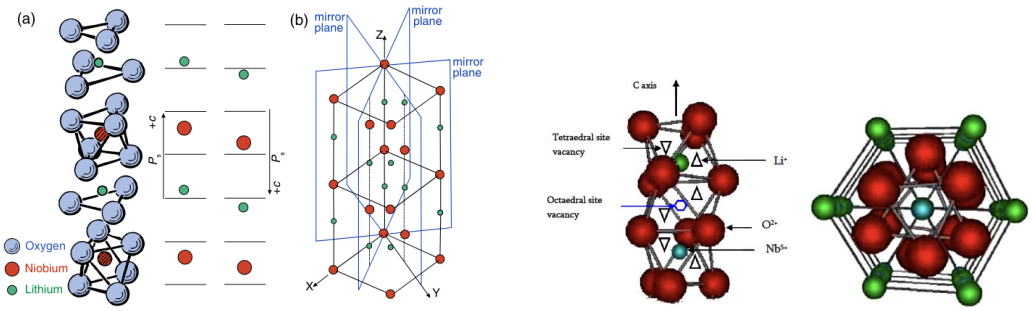

(a) (b)

Figure 1: (a) **left:** The positions of the Li and Nb atoms with respect to the O octahedra in the ferroelectric phase are illustrated in the accompanying diagram. The poling process results in a displacement of the Li and Nb positions, as indicated by the arrows. In the inversion of the spontaneous polarization and the domain orientation, the following definitions are employed: (a) **right:** the standard definition of the X-, Y-, and Z-axes, with Y aligning with a mirror plane [20]; (b) **left:** the primitive rhombohedral cell of LN crystals; (b) **right:** the atomic arrangement of the LN structure along the Z-axis [21].

In the context of radio frequency waveguide technology (RF technology), principally a range of materials, including bulk silicon (Si), silicon nitride (Si_3N4) or indium phosphide (InP), can be employed in conjunction with LN. The advantages of LN can be attributed to a number of beneficial characteristics:
Firstly, LN has one of the highest electro-optic coefficients (r_{33} = 30 pm/V [22]), which makes it an ideal material for electro-optic (EO) modulators, which play a central role in modern telecommunication networks [19]. Secondly, LN exhibits a large second-order nonlinear coefficient (d_{33} = -27 pm/V) [19] and a third-order nonlinear coefficient of $n_2 = 1.8 \cdot 10^{-19}$ m^2/W [19], which is comparable to that of other commonly used optical materials, thereby enabling Kerr comb generation [23]. In addition to second- and third-order nonlinearities, LN exhibits a broad transparency window spanning from the ultraviolet to the mid-infrared spectrum (420 nm - 5200 nm) [19]. In preparation for optical transitions in chapter 2.3, the optical bandgap values (E_{gap}) of LN falls within the range of 3.3 – 4.7 eV (depending on the measurement methods) [24]
Additionally, LN exhibits minimal propagation losses, reaching realistic as low as 0.2 dB/cm [25].

The production of TFLN wafers out of bulk LN employs a process known

as SMART CUT® fabrication [19]. This process is schematically illustrated in Figure 2. The initial step involves defining a cleavage plane is defined in a high-quality LN substrate at the desired film thickness through the use of high-dose implantation of helium $(He)^+$ or hydrogen $(H)^+$ -ions (a). The LN substrate is thus called "donor-wafer" [26]. Subsequently, a Si substrate waver with an oxide layer, the "acceptor-wafer", is prepared (b). Moreover, the LN substrate is bonded to the wafer base, and thermal annealing is applied to split the substrate along the predefined cleavage plane, resulting in a thin film (c) and (d). Further annealing procedures serve to diminish the impact of ion implantation-induced crystal defects, in conjunction with the polishing of the entire chip surface to enhance its smoothness (e).
The aforementioned process can be observed once more in the following Figure 2 [19]:

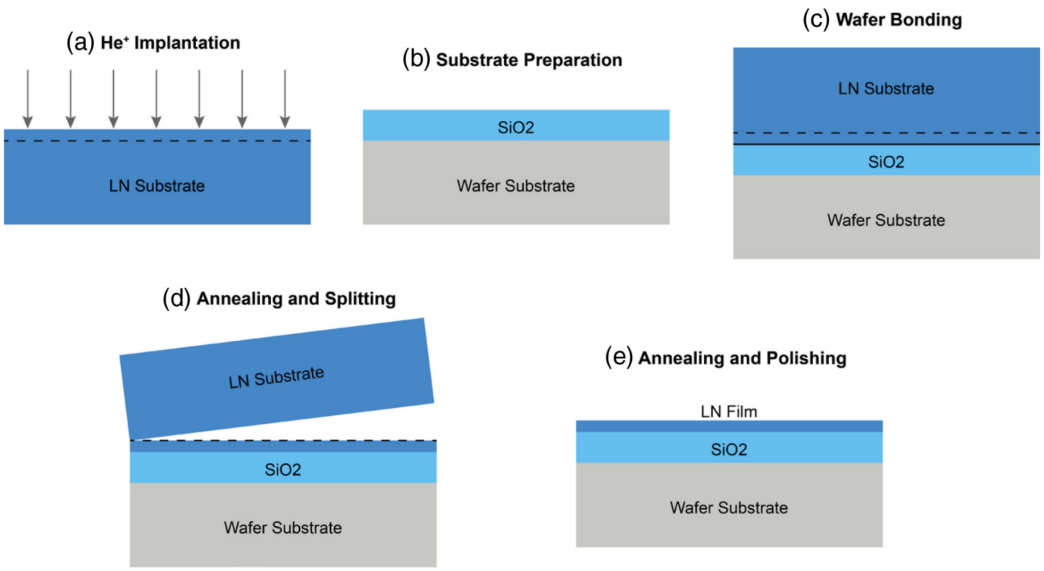

Figure 2: Schematic picture of the Smart-Cut process for LN wafer production, taken unchanged from [19].

Following an initial period of development in the early 2000s [27], high-quality TFLN wafers, produced through ion slicing and wafer bonding, have become commercially available in recent years. The application of novel fabrication techniques has enabled the realisation of nanophotonic LN waveguides, which exhibit the combined characteristics of ultra-low loss and simultaneously high index contrast [28] (as demonstrated in the aforementioned section of part 2.1). In recent years, a set of integrated optical components has been developed on the TFLN platform, including compact and ultra-high-performance

modulators [29], broadband frequency comb sources [30], photon-pair sources [31] and efficient wavelength converters [32]. This platform is therefore suitable for hosting a variety of components, including optical and optomechanical cavities [33], tunable filters [34], acusto-optical modulators [35] [36] and electro-optical modulators [37]. It is accordingly unsurprising that the field of photonic research has high expectations of TFLN as a multifunctional and high-performance platform for integrated photonic circuits, applicable to both classical and quantum applications [19].

2.2 Erbium-Doping

Erbium (Er) is a rare-earth element and lanthanoid with the atomic number 68. The concentration of Er in the Earth's crust is approximately 2.8 ppm, while in seawater 0.9 ng/l, equivalent to 910^{-7} ppm [38] (for comparison: The concentration of Nb in the Earth's crust is 20 ppm [39]). It should be noted, however, that in its natural state, Er is never found in a free elemental form, but only in association with monazite sand ores. The extraction process is currently conducted with the aid of ion-exchange chromatography techniques [40].
When artificially isolated, it displays a silvery-white appearance [10]. However, when present as a salt, such as the erbium(III) nitrate pentahydrate ($Er(NO_3)_3$) used in this thesis, it exhibits some pink fluorescence. Er has a wide range of applications in everyday life. As a salt, Er finds application in the colouring of glass, cubic zirconia, and porcelain. The glass coloured with Er is utilised in a variety of contexts, including the production of imitation jewellery and sunglasses. Er is also utilised in a number of other fields, including metallurgy, where it is incorporated into vanadium as an alloys to enhance mechanical resistance. Nevertheless, the most pioneering application of Er currently is in silica-glass optical fibres doped with Er, which are extensively used in optical communications and laser applications. In this thesis, Er is employed in this very application in the form of Er-doped TFLN-waveguides for telecommunication applications [9].
As proposed by Younesi et al. [9], the method employed for doping TFLN is a low temperature ion exchange process utilising a salt melt of Er. The chips are immersed in melted salt, where ion exchange is conducted by submerging x- and z-cut crystal plates at temperatures between 450°C and 600°C. During the doping process, Er^{3+} ions diffuse from the melt into LN, replacing primarily Li^{+} ions, which outdiffuse into the melted salt. However, it is crucial to acknowledge that the ion exchange cannot be described as a simple replacement process. As a consequence of the rearrangement of the local

environment resulting from the alteration of the valence state, the structure of the LN undergoes a transformation. Consequently, following the incorporation of Er, some structural rearrangements occur in the LN matrix. A detailed account of the doping process will be provided in the subsequent section 3.1.

2.3 Operation Principle of Erbium-Doped Amplifiers

As already mentioned in the introduction, in the context of modern telecommunication, there is a pressing need to reduce fibre loss, particularly in the context of Wavelength Division Multiplexing (WDM). This is a transmission technology that employs a single optical fibre to convey multiple optical carriers of different wavelengths in an optical fibre communication simultaneously [41]. Following years of research, the most suitable transmission wavelength window has been identified as 1260 nm to 1625 nm, which exhibits the lowest dispersion, the least signal distortion and the lowest loss across a range of materials. The wavelength spectrum of an optical fibre can be subdivided into discrete bands, each of which is used as an independent channel with a predetermined wavelength transmission [42]. In accordance with the standards set forth by the Comité Consultatif International Télégraphique et Téléphonique (ITU-T), as outlined in [43], single-mode optical fibres with a band exceeding 1260 nm are classified into six category. The aforementioned bands are as follows: original band (O) (1260 - 1360 nm), extended band (E) (1360 - 1460 nm), and short wavelength band (S) (1460 - 1530 nm). The remaining bands are the conventional band (C) (1530 - 1565 nm), long wavelength band (L) (1565 - 1625 nm), and ultralong wavelength band (U) (1625 - 1675 nm).

As stated by HYC Co. in reference [42], the C-band, which ranges from 1530 nm to 1565 nm, is so designated because it represents the most commonly used conventional telecommunication wavelength. Optical fibres demonstrate the lowest loss in the C-band, thereby conferring significant benefits in long-distance transmission systems. Consequently, C-band fibres are extensively employed in metropolitan areas in conjunction with WDM, long-distance, ultra-long-distance and submarine optical transmission systems, as well as Erbium Doped Fiber Amplier (EDFA) technology. As transmission distances continue to increase and fibre optic amplifiers are employed instead of optical-to-electronic-to-optical repeaters, the significance of the C-band is becoming increasingly apparent. The advent of Dense Wavelength Divison Multiplexing (DWDM), which enables the sharing of a single fibre with multiple signals, has resulted in an expansion in the utilisation of the C-band.

It is evident that despite the minimal losses observed in the C-band and the exceptional properties of LN, the losses cannot be reduced to zero. The remaining losses, which are relatively low, accumulate over longer distances. In order to achieve an amplification, the Er atoms which were doped into the TFLN, experience a combination of excitation and stimulated emission as illustrated in the following Figure 3 (a). As outlined by Heilemann in [44] and Finot in [45], first, the Er within the waveguide are initially stimulated by a pump laser, which emits light at either 980 nm or 1480 nm laser light. This results the optical transition $^4I_{15/2} \longrightarrow {}^4I_{11/2}$ for 980 nm and $^4I_{15/2} \longrightarrow {}^4I_{13/2}$ for 1480 nm by the absorption of the respective photon [46]. The input light at 980 nm with an input power typically ranging from 10 to 200 mW, triggers an excited state, $^4I_{11/2}$, which then transits via phonon relaxations to the metastable state $^4I_{13/2}$ [47].
In the subsequent phase, either a spontaneous or stimulated emission is possible. When focussing on the spontaneous emission, an initially perplexing scenario elucidates, depicted in Figure 3 (b). It can be observed that the photons beeing emitted from the $^4I_{13/2} \longrightarrow {}^4I_{15/2}$ transition during spontaneous emission do not exhibit a single wavelength but rather a broader distribution, with a peak at 1530 nm.
The scientific community is therefore producing a variety of output wavelengths, including 1530 nm [20], 1531.6 nm [48], 1540 nm [49], and 1550 nm [50] or 1562.7 nm [51]. Specifies values of 1530 nm [20], 1531.6 nm [48], 1540 nm [49], 1550 nm [50] and 1562.7 nm [51].

Paschotta [46] suggests that the observed variability can be attributed to the intricate structure of the system. The multi-phonon transition, which is a consequence of the high phonon energies, occurs relatively rapidly, leading from $^4I_{11/2}$ to $^4I_{13/2}$. It can therefore be concluded that each transition requires the involvement of phonons. The upper-state lifetime from the $^4I_{13/2}$ level is in the order of 8 ms to 10 ms, while all higher-lying levels exhibit lifetimes of a few microseconds due to rapid multi-phonon decays. It is similarly conceivable that the energy levels may fluctuate from one location to another, where the experiment takes place, if the external conditions vary under which experiment is conducted. In combination with the different phonon levels inside the atom, insufficient shielding for example against external electric fields (Stark Effect [52]) or magnetic fields (Zeeman-Effect [53]) result in the splitting of the energy levels into smaller units. It is also possible that this variety of energy levels may also influence the wavelength of the light emitted by Er-doped TFLN [54].

To address this issue of a broad wavelength distribution, a so-called "seed laser" is employed to trigger stimulated emission via the transition $^4I_{13/2} \longrightarrow {}^4I_{15/2}$, as outlined in [44] and [45]. This indicates that the photons emitted by the Er atoms following the $^4I_{13/2} \longrightarrow {}^4I_{15/2}$ transition are identical to the seed laser and correspond to the coherence criteria due to the same propagation direction, same wavelength and same phases. With this method, the photons emitted by Er will invariably possess the wavelength of the inputted light [47].

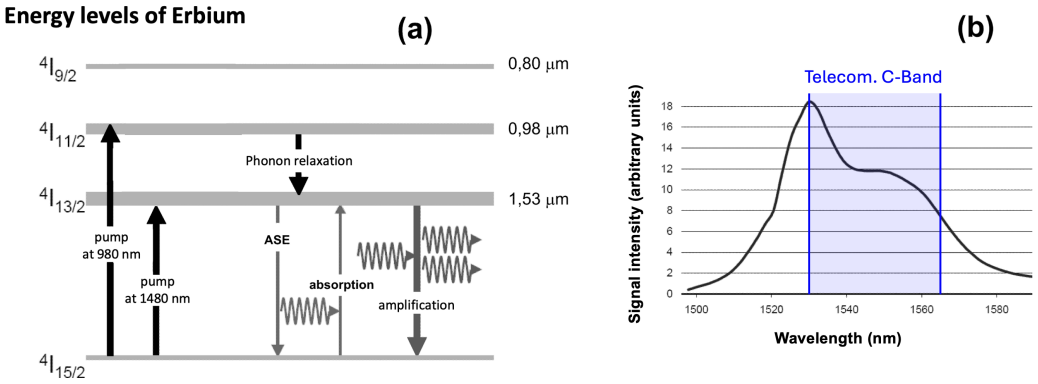

Figure 3: **left:** schematic sketch of the excitation and emission processes during the erbium-doped amplification **right:** sketch of the width of the photon emission while spontaneous emission, as the number of possible wavelengths is greatly increased due to the fine structure. [45]

As a result of the aforementioned process, the application of 980 nm has yielded in the attainment of gains within a range of 5 dB/cm [20] and 6.20 dB/cm [48] and 20 to 30 dB for 1480 nm (here the source just gives the internal net gains) [47].

The following section outlines a technique for doping TFLN with Er. This technique is based on the methodology described in sections 2.2 and 3.1 of the previous text. The objective of this project, which was initiated with this thesis, is to achieve comparable magnitudes using the described technique.

3 Methods and Experimental Setups

This bachelor's thesis presents a number of experimental setups and measurement methods, which are introduced and described in detail in the following sections. The section begins with an overview of the Er doping setup, waveguide fabrication and scanning electron microscopy and energy dispersive X-ray spectroscopy. It then proceeds to present the fibre-coupled, reflection, transmission and free-space setups.

3.1 Erbium-Doping Process

The sample material employed in this thesis is a TFLN-chip, constructed in accordance with the methodology outlined in Figure 2. As illustrated there, 2.2 (right), the chips are contructed with a 525 µm layer of bulk Si, followed by a 4.7 µm layer of silicon dioxide (SiO_2) and a 330 nm layer of TFLN. An overview of the subsequent doping process is provided in Figure 4. The initial stage of the process involves the preparation of the salt mixture, which will subsequently be used to dope the chip. The salt mixture typically comprises 27 g of potassium nitrate (KNO_3) and a variable quantity of $Er(NO_3)_3$. Consequently, a high precision scale weight is employed to reduce the margin of error to approximately 0.010 g. In the event of clumping of KNO_3 or $Er(NO_3)_3$, the material must be crushed and mixed in order to achieve the greatest possible degree of homogeneity. Concurrently, the chips are labeled on their underside using a diamond pen. This procedure must be conducted with particular care to avoid damaging or cracking the chip by applying excessive pressure. Additionaly, all sample chips are cleaned with aceton, CH_3COCH_3 (AC) in an ultrasonic bath to remove the protective layer applied during the production process. The AC is then removed using deionized water and isopropyl alcohol, $CH_3CHOHCH_3$ (IPA).
In the next stage (Figure 4 (a)), the chip is positioned within the salt mixture, ensuring that its surface is entirely covered and that its orientation is such that the bottom side is facing downwards. The doping process is initiated by placing the beaker containing the sample on a programmable heat plate. According to Younesi et al. in [9], the plate is then subjected to tempering, for instance at a temperature of 465°C with a heating rate of 30°C/min. This exceeds the melting temperature of both $Er(NO_3)_3$ (130°C [55]) and KNO_3 (337°C [56]), as observed by [57], resulting in the complete melting of the salt mixture. Later, the remaining larger salt clusters also melt under the applied heat and disperse homogeneously.
As a consequence of Brownian motion [58], the solution is presumed to be homogeneous (Figure 4 (b)) and the doping process occurs as previously

described in section 2.2, with the quantity and distribution contingent dependent on the applied temperature and time. Next, the sample is subjected to a combined process comprising, conducting, annealing, and diffusion, in accordance with a previously defined temperature sequence (Figure 4 (c)). Figure 4 (c) illustrates a typical temperature sequence, which comprises an annealing process conducted in in three stages, with temperatures of 200°C, 300°C and 400°C, for durations of 4 h, 4 h and 23 h, respectively [9]. The notation 200/300/400°C and 4/4/23 h is employed for the sake of simplicity. The temperature differential between the successive annealing stages is maintained at 5°C per minute. It is important to note that the annealing process is a critical phase in the doping procedure. It facilitates the diffusion of Er^{3+}-ions deeper into the TFLN substrate and simultaneously enables the reallocation of damaged crystal structures [9]. As with the doping in the previous step, the parameters shown are sample values that will be optimised later in section 4.1.

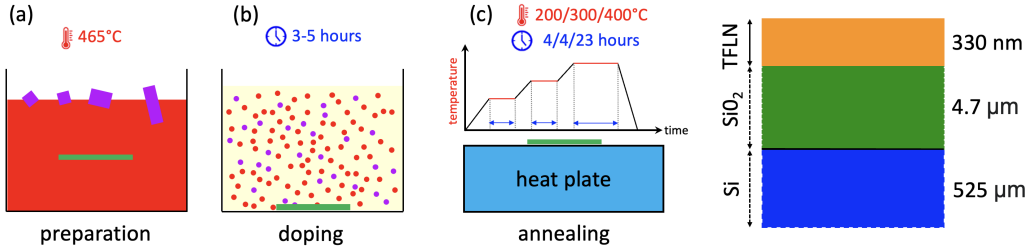

Figure 4: **left:** (a) preparation of the salt-mixture with $Er(NO_3)_3$ and KNO_3 and inserted chip in the beaker, (b) increasing temperature of sample and solution with heat plate, (c) subsequent annealing process with bare chip laying on heat heat plate. **right:** schematic cross section of the waveguide chips. Taken changed from [9]

In order to facilitate the diffusion of Er^{3+} ions into the LN substrate, while simultaneously preventing irreversible damage to the crystal structure, such as the formation of cracks, a number of parameters associated with the doping process will be optimised at a later stage in this work. The variables to be optimised are the quantity of $Er(NO_3)_3$, the temperature at which doping occurs, the duration of the doping process, the temperature and duration of annealing, and the number of annealing stages. All of the aforementioned optimisation steps are conducted in parallel with x- and z-cut TFLN chips. This means that for x-cut, the present crystal plane is the yz-plane of the

LN and for z-cut, the xy-plane.

3.2 Waveguide Fabrication

The production of waveguides is a process that is divided into two distinct phases: design and production. The following sections will analyse these two phases in greater detail.

Waveguide Design

The design of the waveguides was conducted using gdshelpers [59], a flexible open-source Python framework that enables the generation of masks for integrated circuitry. Being available open-source confers a significant advantage, as other commonly used commercial software packages for high-end design are prohibitively expensive. At the software level, the framework includes adapters that facilitate the conversion of arbitrary Shapely objects into gdsCAD/gdspy objects, which are then suitable for use in the subsequent manufacturing process.
This thesis uses the design of Shapely objects, including tapers for hybrid 3D integration, curves and straight lines for waveguides, and further polygons. The Python platform PyCharm CE 2021.3.3 has been selected for use [60]. Figure 5 illustrates the Blender® animations of the chip, while the gds file that serving as the basis for the subsequent fabrication process is illustrated in Figure 6 and Figure 7 depicts the outcomes subsequent to dry etching, as later described in Figure 8.

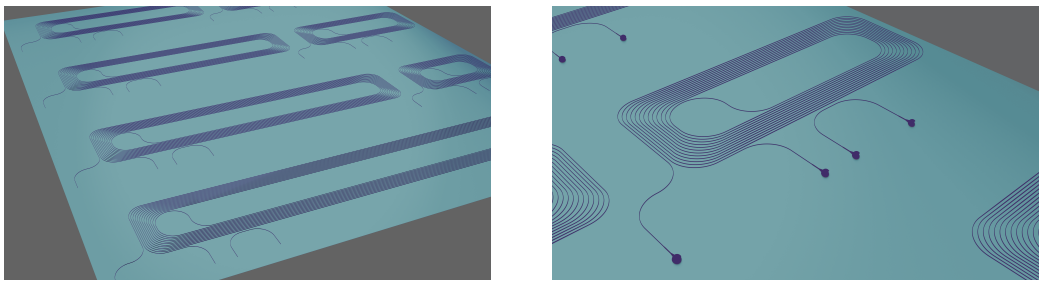

(a) (b)

Figure 5: (a) Illustration of the designed waveguide using BLENDER® version 4.1.1. without 3D couplers, (b) Close view on a small waveguide featuring the 3D couplers for the long loop on the left and the short calibration loop on the right. It should be noted that the conversion to positive and the systematic indexing have not yet been applied in either illustration.

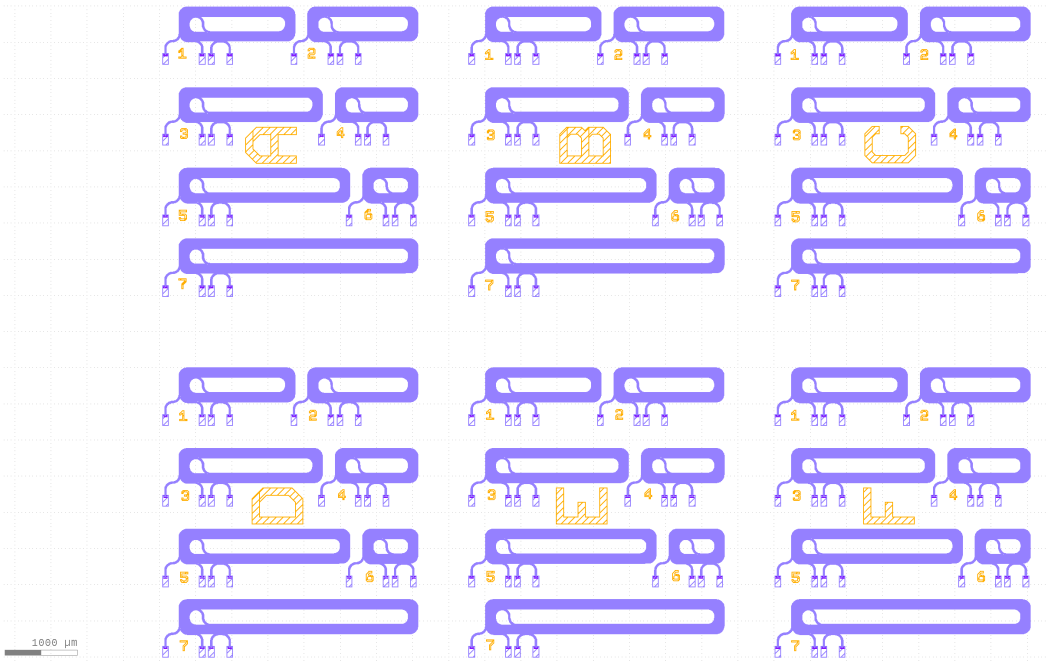

Figure 6: Layout of the waveguide chip containing 6 smaller identical chips.

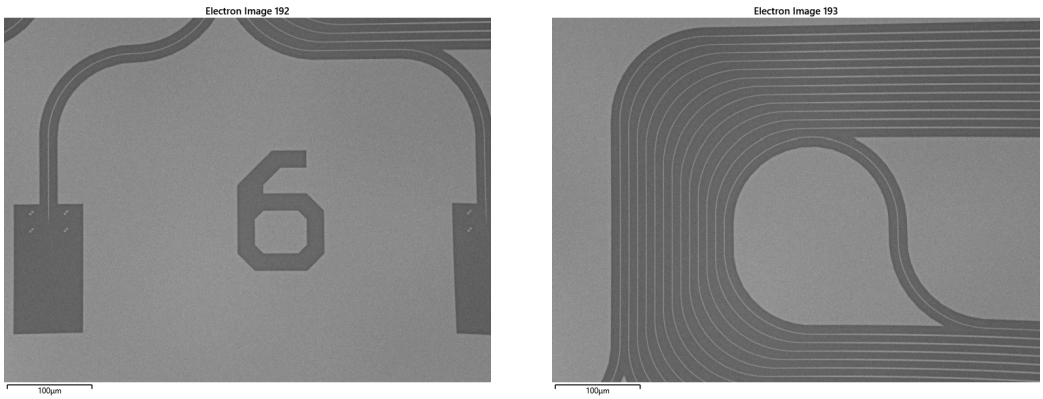

(a) (b)

Figure 7: (a) Coupling region of undoped TFLN waveguide after fabrication, (b) Waveguide loop of the same waveguide region.

Waveguide fabrication

In order to fabricate waveguides out of TFLN, a special technique called dry etching is applied, as described by Bankwitz et al. in reference [61]. The individual steps are illustrated schematically in Figure 8.

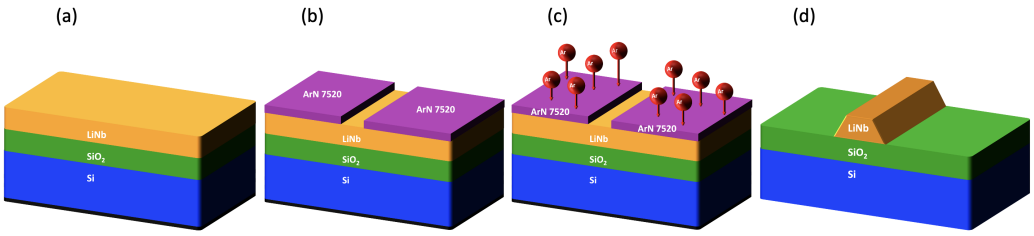

Figure 8: Schematic steps of the "dry etching process" using a positiv resist.

The waveguide structures are patterned onto the TFLN chip using the Electron Beam Pattering Lithography (EBPL) method. As illustrated in Figure 8 (a), the initial configuration comprises a chip, structured as described in section 3.1, onto which a spin-coated positive photoresist (ArP 6520, Allresist GmbH) is applied in accordance with the desired pattern. In comparison to a negative resist, a positive one is more time-efficient and prevents material wastage during the fabrication process. Subsequently, Inductively Coupled Plasma Etching (ICP-RIE) is employed, utilising an optimised argon (Ar) milling process to remove the previously marked areas having the positive resist (Figure 8 (c)), thereby leaving the desired pattern on top of the TFLN layer (Figure 8 (d)). Moreover, the etched sample is subjected to an additional RCA-1 etching process to eliminate the potential for potential redepositions resulting from the employed sputtering technique. As can be observed in Figure 8 (d), the final waveguide sidewalls are angled. However, this angle, typically between 60 and 63 degrees for both sides [62], has no significant bearing on the subsequent development of this thesis. Potential avenues for their removal or optimisation can be found in the existing literature [62] [63].

3.3 Electron Microscopy

One of the primary techniques employed in this thesis was electron microscopy. The technique is used to gather data regarding surface quality and to measure waveguide proportions, as well as to determine chemical composition through the use of Energy Dispersive X-Ray Spectroscopy.
Electron microscopy represents one of the three principal techniques employed in the field of microscopy. While the magnification of Optical Microscopy (OM) is based on visible light and that of Atomic Force Microscopy (AFM) on atomic forces [64], the electron microscope employs electron emission for imaging its samples.
All Scanning Electron Microscopy (SEM)-measurements were conducted us-

ing the ZEISS Gemini 560, all Scanning Transmission Electron Microscope (S/TEM)-measurements with a Thermo Fisher Scientific FEI TITAN Themis G3 60-300 and the necessary Focused Ion Beam (FIB)-preparation for the S/TEM was conducted with the Zeiss Cross Beam 540. The Energy Dispersive X-ray Spectroscopy (EDS) detector is an Oxford instruments AZtec live powered by Ultim® Max [65].
The following chapters provide an overview of the functions of the individual devices. For a more comprehensive understanding of the subject matter, please refer to the referenced literature.

3.3.1 Scanning Electron Microscopy

Electron microscopy can be employed in two distinct operational modes. One such instrument is the SEM, which is capable of magnifying a structure up to 3.000.000 times its original size [66].
The following steps, as described by Mohammed et al. in [67], will present a description of the working principle of an SEM. In the initial stage, an electron beam with an energy scale between 100 and 30.000 electronvolts is generated typically through thermal emission. The considerable spot size of the generated beam presents a significant challenge in achieving a sharp image. Accordingly, the solution in the SEM is to utilise multiple lenses in order to focus the electron beam.
With a final size of less than 10 nm, the beam makes contact with the specimen surface. By moving the beam with the aid of scan coils over the surface of the specimen, a rectangular raster is produced. Upon making contact with the specimen surface, the Primary Electrons (PE) engage in interactions with the Coulomb fields of the specimen material elements. This results in deflection and Backscattering Electrons (BSE), accompanied by a reduction in their energy or the generation of Secondary Electrons (SE) through the release of electrons from a shell. Subsequently, both types of electrons emanating from the specimen are either detected by an Everhart-Thorlay detector (ET) [68] or scintillators and semiconducting materials [69]. The data is then processed with computers in order to display the final image to the user. To enhance the quality of the image, the user has a number of options for improving the image quality, including adjusting the brightness and intensity, increasing the magnification by modifying the working distance[1] or increasing the acceleration voltage of the electron beam up to 30 keV [67].

[1] The working distance describes the distance between the last lens of the lens apparatus and the specimen surface [67].

3.3.2 Scanning Transmission Electron Microscopy

The S/TEM represents a second operational mode of electron microscopy, which will be briefly outlined here as its deployment was confined to a single measurement during the course of the thesis. Further information can be found in references [70] and [71].

As the name implies, the S/TEM operates in a manner analogous to the SEM, with the crucial distinction being that the incident electron is not reflected by the sample surface, but rather penetrates the specimen and is detected by a detector situated behind the sample. Accordingly, the applied acceleration voltage of the electrons is 10 times greater than the maximum of 30 keV applicable with the SEM, namely 300 keV. However, the specimen must be of a minimal thickness to guarantee the transparency of the material for electrons. The thinness of the specimen is achieved by utilising the FIB-method, which involves the initial removal of small sections of material from the sample and subsequent reduction of their thickness [72]. To increase the energy of the incoming electron beam once more, the beam is focused so that its diameter is decreased down to a few nanometres. A lens system then scans the specimen's surface or cross-section. The detection of the penetrated electrons and the signal procession work similarly to the SEM, with the difference being that the detector is placed behind the specimen instead of over it as previously already mentioned [70] [71].

3.3.3 Energy Dispersive X-Ray Spectroscopy

As stated above, EDS is a method for determining the elemental composition of a substance using electron microscopy [73]. This section is divided into two parts: the generation and detection of characteristic X-rays.

Generation of Characteristic X-rays

As indicated by its designation, the EDS is designed to operate with characteristic X-rays. The X-rays are produced by the acceleration of electrons (PE), that collide with the surface of the observed sample. In the surface atoms, the incoming PE possess sufficient energy to ionise the atom by forming electron wholes in the core-shell region. The subsequent filling of this vacant space is conducted by an outer shell electron, which assumes the inner position and releases its surplus binding energy. This energy is then emitted as characteristic X-rays or transferred to Auger electrons, which will not be discussed further at this point. Additional information can be found in the following references: [74], [74] and [75].

X-rays are designated by the shell in which the aperture is formed (from the interior to the exterior, K, L, M, N, O, and so forth) and from where the trailing electron is emitted. The shell number is indicated by the Greek letter alpha (α), beta (β), or gamma (γ), respectively, for the first, second, and subsequent shells. It is essential to recognise that shells with a higher quantum number, n, divide into more subshells, thereby facilitating the potential for a greater number of spectral lines. However, due to the resolution limit, only a few transitions are resolved and are of relevance. For example, $K_{\alpha 1}$ and $K_{\alpha 2}$ or $L_{\alpha 1}$ and $L_{\alpha 2}$ are indistinguishable and occur as one peak). The existence of spectral lines is contingent upon the atomic number of the material under observation. For atomic numbers Z=10, the K-lines begin to split into $K_{\alpha 1}$ and $K_{\alpha 2}$, while for atomic numbers above Z=20, L-lines become visible. In the range of atomic numbers Z=40 and above, the first M-lines emerge. It is evident that there are notable differences in the intensity of the observed spectral lines. For example, in copper, the intensity of the $K_\alpha : K_\beta$ ratio is approximately 10:1 while the ratio of the strongest L-lines is approximately 10:7:2 [76].

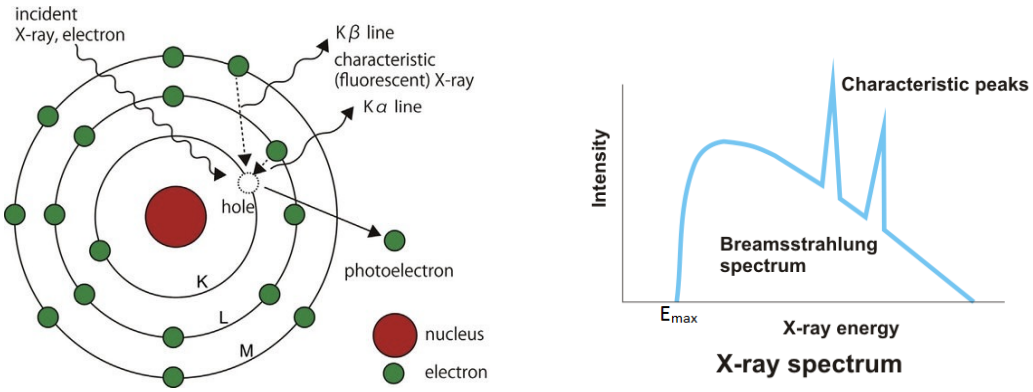

(a) (b)

Figure 9: (a) Schematic visualisation of production of characteristic X-rays [77] (b) X-ray spectrum including characteristic X-rays and Bremsstrahlung-X-rays [78].

However, in an EDS signal, the characteristic X-rays are never observed in their pure form. Rather, they are always present in combination with Bremsstrahlung, providing a continuous background spectrum [76], as illustrated in Figure 9 (b).

X-ray Detection with SEM

The fundamental principle of an EDS detector, as elucidated by Bernardi in [76], is to transform the incoming X-ray energy from the specimen into a voltage signal. The detector is composed of a thin window that serves to safeguard the vacuum within the apparatus, a semiconductor detector that is coated with narrow gold electrodes, an attached Field-Effect-Transistor (FET) a pulse processor, and finally, a Multichannel Analyzer (MCA)).
The interaction of X-rays with the detector results in the production of electron-hole pairs. By applying a voltage difference between the front and back sides of the crystal, these charges are driven in opposing directions. Upon reaching the electrodes, the charges are converted by the FET into voltage pulses, which are subsequently processed and assigned as a count in the MCA. The MCA is typically configured to accommodate up to 4096 channels. However, it can also be reduced manually to increase the processing speed if the signal quality must not be the highest standard.
A longer processing time will always result in an improved spectral resolution and peaks with minimal Full Width at Half Maximum (FWHM), but will also lead to a larger dead time[2]. The dead time is expressed as a percentage, with a recommended value in the range of 15% to 50%. If the specified range is exceeded or undershot, the quality of element detection is significantly diminished.

In accordance with Moseley's law, the energy of K_α X-rays is proportional to $(Z–1)^2$. Therefore, for atoms with a greater atomic number, the applied acceleration voltage for the PE beam must be increased in accordance with the aforementioned relationship [76]). Figure 10 illustrates the individual K_α and L_α values for all elements of the periodic table. By detecting these spectral lines with the aforementioned techniques, a clear assignment of a chemical element is possible.

[2]The term "dead time" is used to describe the period during which the EDS system is unable to register incoming X-rays due to the ongoing processing of the preceding pulse.

Figure 10: Periodic table of elements with characteristiv elements necessary for EDS evaluation. The red marked elements (potassium (K), Nb, Er, Si, carbon (C), nitrogen (N) and O) are of special importance for this thesis, taken modified from [79].

This thesis primarily focuses on the elements K (K_α= 3.31 keV); Nb (K_α= 16.58 keV), Er (K_α= 6.94 keV), Si (K_α= 1.73 keV), C (K_α= 0.28 keV), N (K_α= 0.39 keV) and O (K_α= 0.52 keV). It is recommended that the applied acceleration voltage for the incident electron beam should be at least equal to the highest K_α energy of all elements that are to be detected. However, it is advised that the K_α value should be doubled in order to ensure a high resolution and a sufficient number of counts in the detection parts. In order to increase the number of counts and thus the quality of the EDS signal, it is necessary to optimise the previously introduced parameters, including the acceleration voltage and the working distance, in order to achieve the highest possible energy resolution. This may require a certain investment of time during the measurement process, but it is of the utmost importance that the EDS is able to develop its full potential.

It should be noted that EDS can be employed in an electron microscope utilising both the SEM and S/TEM mode. In a SEM, the chemical composition can be determined in two dimensions (2D), which precludes the generation of information regarding the distribution or depth of individual elements beneath the sample surface. To obtain this information as well, it is

necessary to investigate a FIB-prepared part of the sample, which has been cut out of the specimen, using the S/TEM mode as previously described.

3.4 Setups

In the following section, the aforementioned setups are presented for further examination.

3.4.1 Fibre-Coupled Setups

The two setups described in the following section 3.4.1 and Figure 13 are designed to facilitate the free external movement of the chip of interest on two NFL5DP20S Thorlabs linear translation stages in the x- and y-directions. The incoming laser light is connected via Thorlabs SM 780 HP fibres with a SQS fibre array made with parts from Thorlabs. The fibre array is mounted on an aluminium (Al) arm at an angle of 8 degrees, which compensates for the flattened underside of the SQS fibre arrays. To align the possible chip structures parallel to the fibre array, a Thorlabs CS165MU/M microscope with an OSL2 fibre illuminator light source connected to a computer is used.

Reflection Measurements
A central experiment designed to test the excitation of Er in Er-doped TFLN chips for amplified spontaneous emission by irradiating the surface of a bare chip without any waveguide structures with light at 980 and 1480 nanometres. This is expected to result in the excitation of the $^4I_{11/2} \longrightarrow ^4I_{13/2} \longrightarrow ^4I_{15/2}$ and $^4I_{13/2} \longrightarrow ^4I_{15/2}$ transitions. In order to serve as laser sources, two distinct devices were employed: a TOPTICA Continuously Tunable Single-Frequency Diode Laser CTL, in conjunction with a TOPTICA Digital Laser Controller DLC pro (for 980 nm) and a SANTEC Tunable Semiconductor Laser TSL-770 (for 1480 nm). As illustrated in Figure 11, the emitted light was coupled into fibres leading into a Thorlabs 6015-3-APC S/N-10256041 circulator. Subsequently, the light was directed onto the chip via the fibre array at a distance of a few millimetres.

The reflected and emitted light from the chip was recorded with the same fibre and subsequently directed into the circulator. The 980 nm light and the emitted 1550 nm light are separated from the input light by the circulator and directed into a further fibre. The light is then conveyed via a fibre optic cable to an ANDO AQ6330 Optical Spectrum Analyzer (OSA). Given the technical specifications of the OSA, any reflected 980 nm light was not

detected, as the OSA's wavelength range stays between 1200 nm and 1700 nm. Figure 12 shows the practical implementation of the proposed structural design.

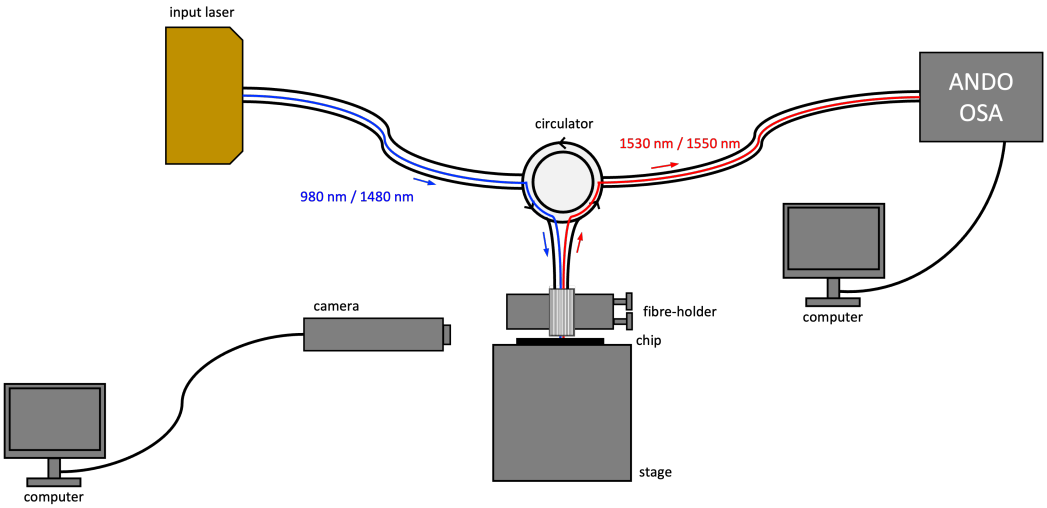

Figure 11: Schematic sketch of the fibre coupled setup.

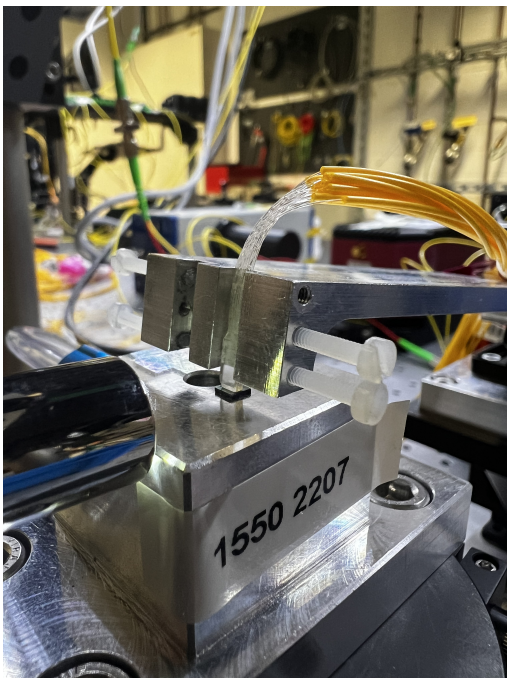

Figure 12: Picture of the fibre coupled setup.

Transmission Measurements

The objective of this part of the study was to identify the optimal doping parameters for TFLN, which would combine the maximisation of stored Er-ions with the maximum signal amplification via stimulated emission in TFLN waveguide structures. However, it was not considered that the optimal amount of Er during the doping process might be the optimum for the actual transmission of 980 nm and 1550 nm light, which is the latter core utilisation of the waveguide. An increased concentration of doped Er ions inevitably gives rise to an augmented number of scattering centres on the other. In light of the considerations pertaining to the concentration of Er and the quality of the surface, the transmission characteristics assume a pivotal role in the context of the intended late waveguide utilisation. It is imperative that they are not overlooked under any circumstances.

This configuration shown in Figure 13 is analogous to that delineated in section 3.4.1. In addition to the mounting on the linear translation stages, the chip is affixed to the substrate by suction with a vacuum pump, thereby improving the stability of its position. The laser light is coupled from the fibre array into the waveguide structure via 3D couplers made of polymer [80], [81] and [82], which were printed onto the chip with the help of the nanoscribe Quantum X align [83]. The input lasers employed are TOPTICA CTL lasers with wavelengths of 910 nm to 980 nm and 880 nm to 940 nm. By moving the fibre array in a controlled manner below a millimetre over the coupler, the laser light is coupled inside the waveguide. The exit 3D couplers are invariably positioned a multiple of 127 µm (in accordance with the internal group convention) in proximity to the input one. The resulting signal was then captured by a data acquisition system and subsequently analysed by a non-commercial Python Graphical User Interface (GUI). Subsequently, further alignment was conducted manually, with the stage being moved while the live transmission signal was monitored using the GUI. Furthermore, the polarization of the input laser signal was optimized using a Thorlabs FPC030 manual fiber polarization controller.

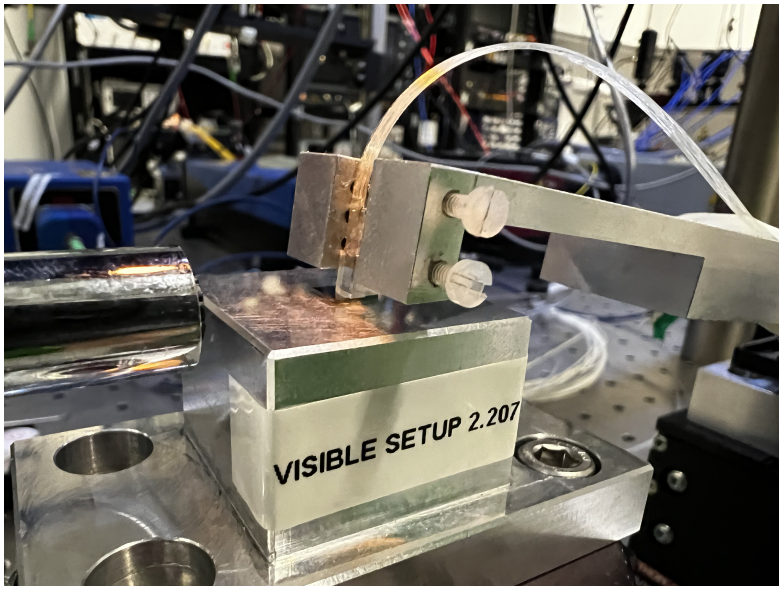

Figure 13: Sideview of the stage the waveguide is placed below the fibre array. For distance control, a camera is used on the left hand side.

3.4.2 Free-Space Setup

In contrast to the previously introduced fibre-coupled configuration, the free-space configuration primarily employs free-space optics, enabling the utilisation of higher laser input power with the objective of overcoming material losses, which are postulated to be the primary challenge of the fibre-coupled configuration. The entire apparatus is situated on a Newport RS 2000 Sealed Hole Table Top with a Tuned Damped optical table. The input laser was a Mai Tai HP One Box Ti:Sapphire ultrafast laser, combined with a GWU UHG-Series Puls Picker, emitting 8 MHz pulses. In Combination with a Ultrafast Harmonic Generator, the acusto-optical modulator technique was employed to achieve the desired pulse deflection. This involved the application of a brief radio-frequency pulse to the acusto-optical modulator, which resulted in the targeted pulse being deflected into a slightly modified direction. The deflected pulses were then able to pass an aperture, whereby the other undeflected pulses were blocked [84].

The finalised laser light is then directed into a Thorlabs optical cage system (Figure 14), where it is steered by a series of Thorlabs dielectric mirrors. Subsequently, the beam path is directed through beam splitters, ultimately entering a Thorlabs GVS002 TSH27101-X Small Beam Diameter Scanning Galvo System, which enables the systematic scanning of the entire chip sur-

face with the laser. To ensure that the beam hits the chip at the focus point and on the designated areas, a white-light source in combination with a camera is used. Following that, the laser beam is reflected by the surface of the sample chips and passes through a Mitutoyo 50x Plan Apo NIR objective before reentering the cage system. Afterwards, the beam passes through a second beam splitter, resulting in a deflection of the beam into the second branch of the cage system. In consideration of the dimensions of the laser beam, which has a maximum diameter of 1.2 mm, it is postulated that the possible emissions of 1550 nm light represent a beam with a diameter that is below the input. It is thus necessary to expand the diameter to that of the free-space fibre coupler in order to maintain a matching mode field diameter for the free space and fibre. This is achieved by utilising a bespoke telescope comprising two lenses, with focal lengths of 75.0 mm (Thorlabs AC254-075-B-ML) and 200.0 mm (AC254-200-A-ML), respectively. In accordance with the geometrical optics, the expansion is determined by:

$$\text{expansion} = \frac{\text{beam diameter}_{\text{final}}}{\text{beam diameter}_{\text{initial}}} = \frac{\text{focal length}_{\text{final}}}{\text{focal length}_{\text{initial}}} \tag{3.1}$$

So the laser light coming collimated from the chip with a maximum beam diameter of 1.2 mm gets expanded by the factor 2.67. To align the beam coming from the chip, a technique called “beam-walking“ was applied with the two mirrors shown in Figure 14. In the beam-walking method, the mirrors are pre-aligned in small steps in conjunction with pinholes in order to guide the laser beam in concentric circles around the target and thus move it step by step to the target point. Next, the laser light is coupled with an additional second laser from the opposite side, in addition to the beam already emanating from Mai Tai. This results in the formation of a beam from both sides, which is then superimposed on both mirrors by means of the two mirrors. Following the introduction of two additional mirrors for alignment purposes, the secondary beam is then coupled into a fibre using a Thorlabs PAF-X-15-C fibre coupler. Subsequently, the fibre is linked to the ANDO AQ6330 OSA, which was already utilised in the fibre-coupled configuration. In order to increase safety during the time-consuming alignment process, a pre-alignment process, where a CPS532 diode laser operating at 680 nm, anodised CPA Al alignment targets and a VRC2 laser viewing card were employed instead of the Mai Tai laser itself. A fine alignment of the measuring arm with 1550 nm light had to be omitted due to a lack of time and equipment.

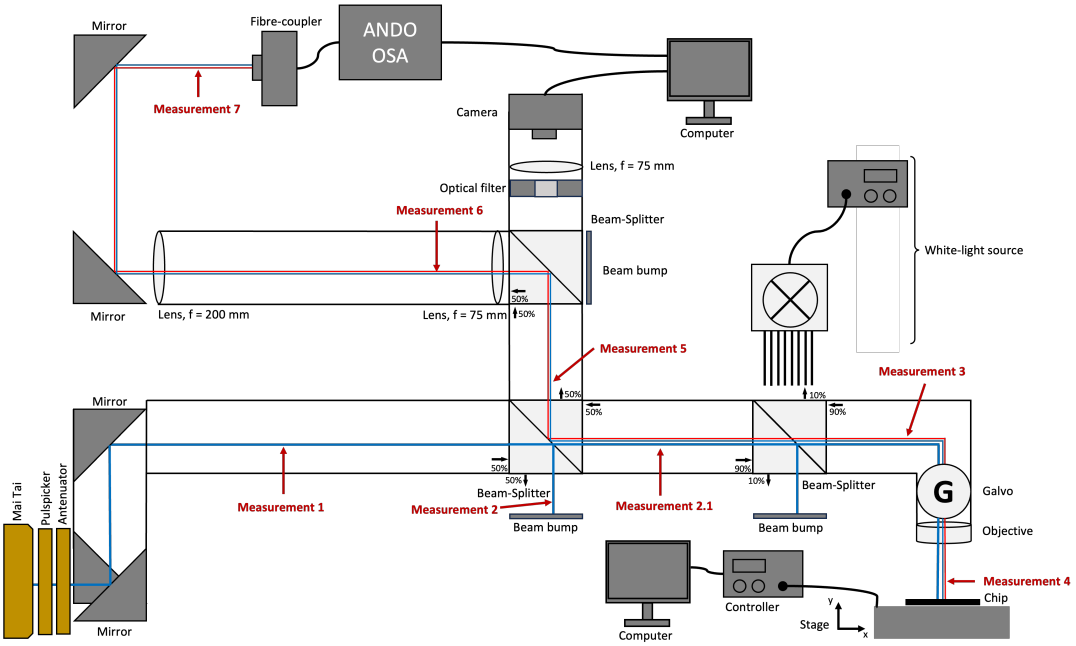

Figure 14: Schematic sketch of the free-space setup.

4 Results

In the following results section, the optimised parameters, observations and challenges during the doping process are first explained. The second part then deals with quantitative measurement series that were carried out with the doped chips.

4.1 Optimisation of Erbium-Doping Process

In order to optimise the initial doping process described in reference [9], a series of variables have been investigated, including the concentration of KNO_3:$Er(NO_3)_3$, the temperature at which doping occurs, the temperature at which annealing takes place, and the method of cleaning the chip surface. Subsequently, all modifications were examined via SEM and EDS to ensure the highest possible concentration of Er in the TFLN layer, while simultaneously maintaining the integrity of the chip surface, preventing any cracks or damage. This delicate equilibrium has consistently represented a significant challenge, with the ensuing outcomes being subjected to detailed examination in the forthcoming sections.

In the following section, a notation for the classification of chips with their respective doping parameters is presented. This notation is illustrated in 15.

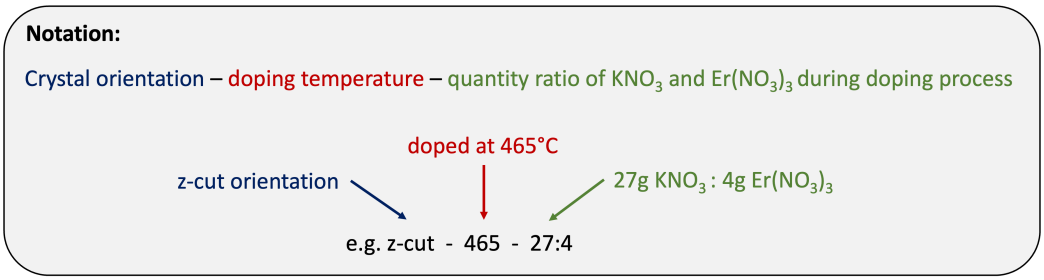

Figure 15: Classification of chips according to their individual doping parameters.

In light of the previous applications of TFLN in diverse contexts, it remains uncertain, whether the preference aligns with the utilisation of x-cut or z-cut chips. This ambiguity persists despite the references in [9], [50], [48] and [20]. Therefore, in all subsequent adjustments of the doping parameters, all changes were applied to both x-cut and z-cut simultaneously in order to ascertain whether this had any impact.

We will begin by discussing the surfaces of the chips. Cracks in TFLN may occur during fabrication due to various factors. Primarily, Er ions are with Z=68 much larger than the Li- (Z=3) or Nb-ions (Z=41) they replace in the crystal lattice. This discrepancy in size can result in strain within the crystal lattice, necessitating adjustments by surrounding atoms to accommodate the larger dopant ion. Should the strain exceed the material's capacity to accommodate it, the doping process may result in the formation of cracks. Secondly, doping can alter the local thermal expansion properties of the TFLN. If the regions in which doping has occurred expand or contract at different rates to the surrounding areas, which may be less strongly doped, differential stresses can build up in response to temperature changes. This phenomenon can be observed even when slow heating and expanded cooling phases are employed after high-temperature doping processes, as discussed in section 3.1). Such stresses can subsequently result in the formation of cracks.

It could be argued that the introduction of a dopant into a crystal results in distortions and the creation of defects in the lattice. Such defects can function as stress concentrators and serve as the initial points of crack propagation. However, this detrimental effect can be mitigated through the implementation of a straightforward procedure. The process of annealing. As previously outlined in section 3.1, annealing represents a widely employed technique for the restoration of the intact crystal structure.

Erbium Doping Concentrations

Initially, the objective was to optimise the parameters by varying the concentration ratios of the employed KNO_3 and $Er(NO_3)_3$. The concentration of KNO_3 remained constant, while the $Er(NO_3)_3$-concentration was varied between 0.2 g, 0.3 g, 0.4 g, 0.6 g, 0.8 g, 1.0 g, 2.0 g, 3.0 g, 3.1 g and 4.0 g. The doping temperature was initially set to 450°C, while the annealing temperature was set to 200/300/400°C as described in section 3.1. The quantity of Er that succesfully diffused into the TFLN behaves according to Figure 16. An extendend overview over all applied parameters and their effects can be found in the appendix section 7 in Figures 31 and 32.

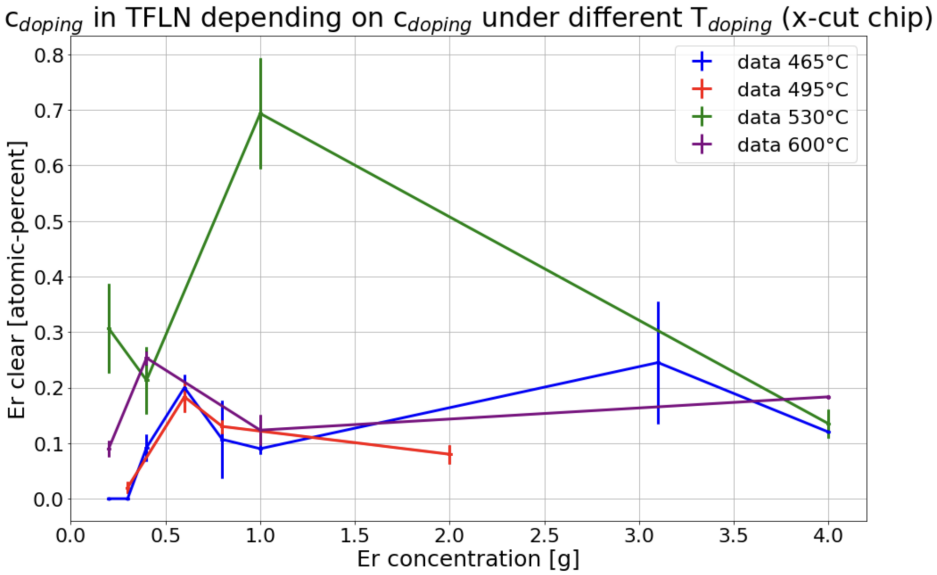

Figure 16: Er concentration in TFLN depending on doping-concentration under different doping temperatures in x-cut.

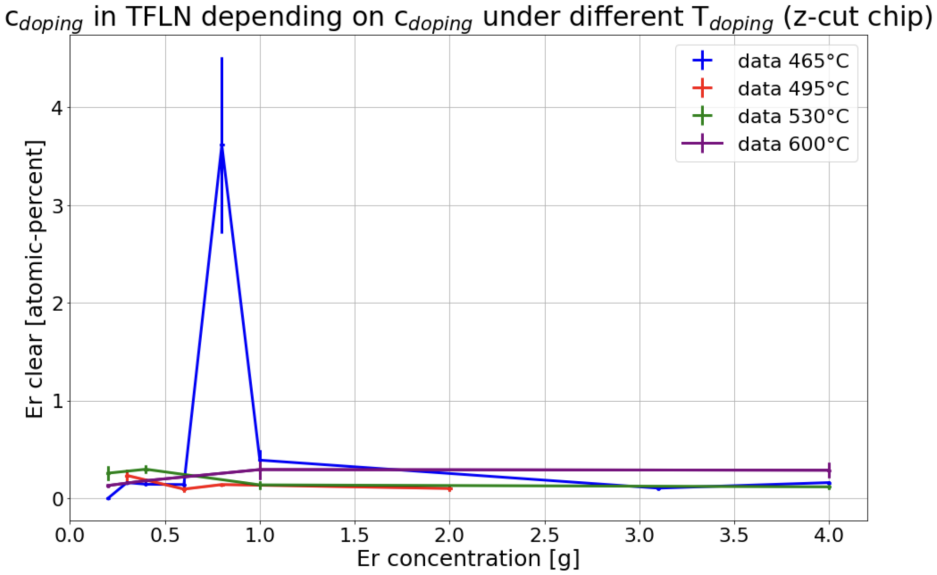

Figure 17: Er concentration in TFLN depending on doping-concentration under different doping temperatures in z-cut.

While for the z-cut the Er concentration remains largely constant at 465°C (neglecting the fourth measurement point, which appears to be an error measurement), the x-cut chip appears to have a local maximum around 0.6 g

$Er(NO_3)_3$.
One potential explanation for the discrepancy between the x- and z-cut is the crystal structure of the lithium niobate from section 2.1. In the z-cut, there are channels in the z-direction within the lithium niobate, which facilitate both the diffusion of erbium in and the diffusion of lithium out. In contrast, the x-cut configuration necessitates that the ions traverse the compact lattice structure with considerable difficulty.

The SEM measurements revealed the emergence of cracks at concentrations of 0.2 g $Er(NO_3)_3$ and concentrations above 0.8 g. This might happen, because too much Er, which has a larger radius than Li subsitutes too many Li-ions in the TFLN, which irreversibly damages the stability of the crystal structure. Two illustrative images are presented in Figure 18 for reference. The overlapping area of high Er concentrations and simultaneously undamaged chip surfaces is therefore around 0.6 g $Er(NO_3)_3$.

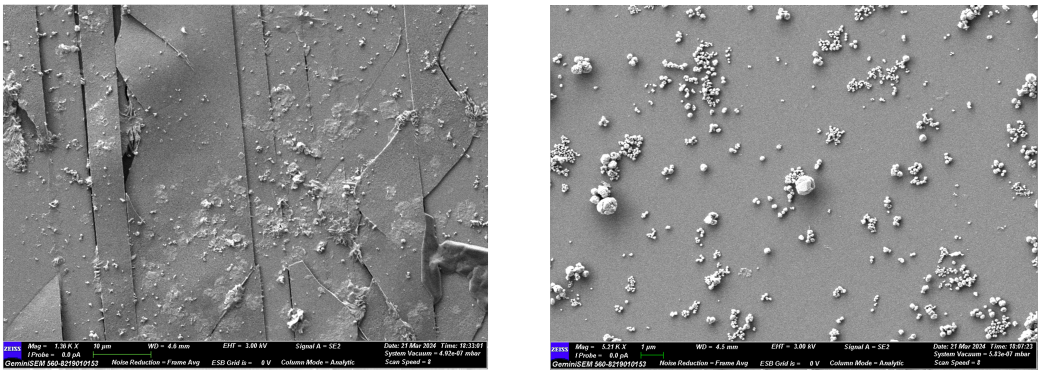

(a) (b)

Figure 18: (a) x-cut-495-27:0.8 chip with cracks along the z-axis of the TFLN, (b) undamaged surface of a x-cut-465-27:0.6 chip.

Doping Temperature

Furthermore, the impact of the doping temperature on the doping success was investigated. As illustrated in Figure 16, the doping process was conducted at temperatures of 495°C, 530°C and 600°C in addition to the original temperature of 465°C. While the achieved Er concentration for z-cut remained relatively constant, the formation of the local maximum around 0.6 g $Er(NO_3)_3$ was confirmed for x-cut. The use of SEM revealed that all chips subjected to temperatures exceeding 530°C exhibited the formation of cracks. These findings suggest that a $Er(NO_3)_3$ concentration of approxi-

mately 0.6 g and a doping temperature of 465°C may represent the optimal parameter. As a consequence of the preceding analysis of the distinctions between x- and z-cut, it can be observed that disparate patterns of fracture occur in the TFLN between the two cutting types. In the case of x-cut, the TFLN fractures in a manner that is aligned with the z-axis, resulting in the formation of cracks that run parallel to one another. In contrast, the z-cut configuration exhibits a lack of a pre-defined fracture direction within the x-y plane, resulting in a disordered fracture pattern. Figure 18 (a) already showed such a parallel pattern for a x-cut chip (x-cut-495-27:0.8), while the following Figure 19 shows the pattern of a z-cut chip (z-cut-450-27:3).

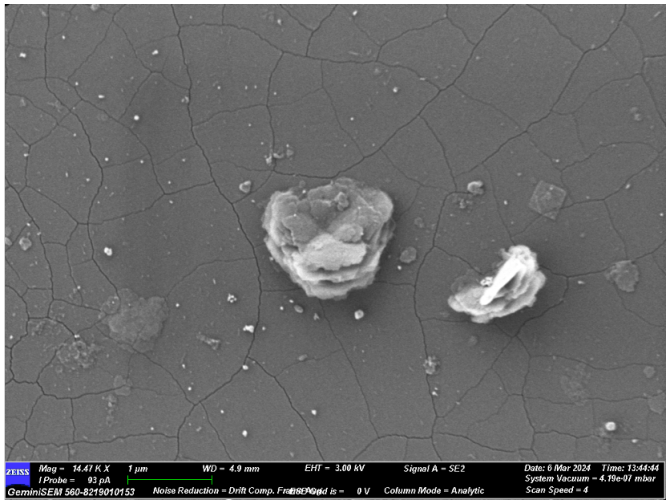

Figure 19: z-cut-450-27:3 chip with its cracks in the x-y-plane.

Annealing Temperature

In the subsequent measurement series, 0.6 g $Er(NO_3)_3$ and a doping temperature of 495°C were take as optimal parameters based on the results of the previous series. Instead of a gradual annealing process at temperatures of 200/300/400°C and durations of 4/4/23 h, annealing was conducted for 23 hours at temperatures of 450°C, 500°C, 550°C and 600°C. As stated in reference [9], the duration and thermal intensity of the annealing process have no impact on the amount of Er present in TFLN. This hypothesis was validated through EDS measurements. The objective was to assess the quality of the film. In relation to the reparative function of annealing, it was hypothesised that a higher annealing temperature might facilitate superior repair of the crystal structure. Consequently, the objective of the measurement series was to ascertain the maximum annealing temperature, in order to prevent cracking of the chip surface. It was observed that 450°C represents the upper limit

for annealing, as temperatures above this threshold resulted in the formation of cracks or, in some cases, extensive damage, which ultimately led to the complete destruction of the TFLN layer.

Erbium Diffusion

As already mentioned several times in the above chapters, low temperature ion diffusion is used as a doping method. Now the question naturally arises as to whether diffusion movements of Er can also be recognised within the TFLN at room temperature and whether the Er concentrations change in some places or even on an entire chip. With the help of callibration measurements, the inaccuracy of the EDS was first determined, but this is in the low single-digit percentage range and therefore has no significant effect.
Firstly, it was generally observed that for chips that were doped at intervals of 1-2 weeks and subsequently analysed, all of them exhibited comparable values of Er among each other and to those observed in earlier measurements, where a Er-concentration between 0.2 and 0.8 $\%_{atomic}$ were measured. In order to investigate whether diffusion movements take place over a longer period of time after doping, several series of measurements were carried out.

The initial stage of the investigation involved a prolonged observation period, spanning over two weeks, during which EDS determinations were employed at each pivotal stage of the doping and annealing procedure. This was followed by an additional week of monitoring the Er-concentrations in the TFLN-layer. As illustrated in Figures 20 and 21, the Er concentration was subjected to a comprehensive analysis according to various criteria. In Figure 20, a distinction was first made between the consideration of x-cut and z-cut chips, in each of which a further distinction is then made between the doping concentrations of 0.2 g and 0.6 g Er. In Figure 21, after division into x- or z-cut, a distinction was made not by doping concentration but by position on the chip. The exact positions are shown in the legend of Figure 21. The percentage number always indicates the percentage of the measurement points carried out under the respective criterion for which an increase, decrease or stagnation of the Er concentration was observed. The percentage value was each determined after 4 to 5 measurements at the same position on the chip within the surveillance period. It is evident that the concentration of Er exhibits a consistent or increasing trend over time in 70% to 100% of all measurment positions. The instances in which the quantity of Er diminished, constituted an average proportion of 12% to 18% (depending on the criteria).

It was assumed that Er might migrate from the centre of the chip to the far edges, potentially utilising the canals within the crystal structure. This

structure described in section 2.1 renders the x-cut chips particularly intriguing, as the TFLN layer remains in the y-z plane of the LN structure due to the specific cutting process. It can therefore be hypothesised that Er may be able to move more easily through these canal structures than z-cut TFLN, which remains in the x-y plane.
Consequently, the locations where the long-term measurements were conducted were selected with particular attention paid to both the central and peripheral regions of the chip. However, as illustrated in Figure 21, no discernible pattern emerges. Moreover, EDS line scans were conducted with a highly precise sampling rate, with each scan taking several minutes. These scans were carried out in both the central areas of the chip and the edges and combined in order to detect possible gradients of Er over the chip surface. However, no such gradient was measurable, and thus the results did not support the hypothesis of further Er diffusion.

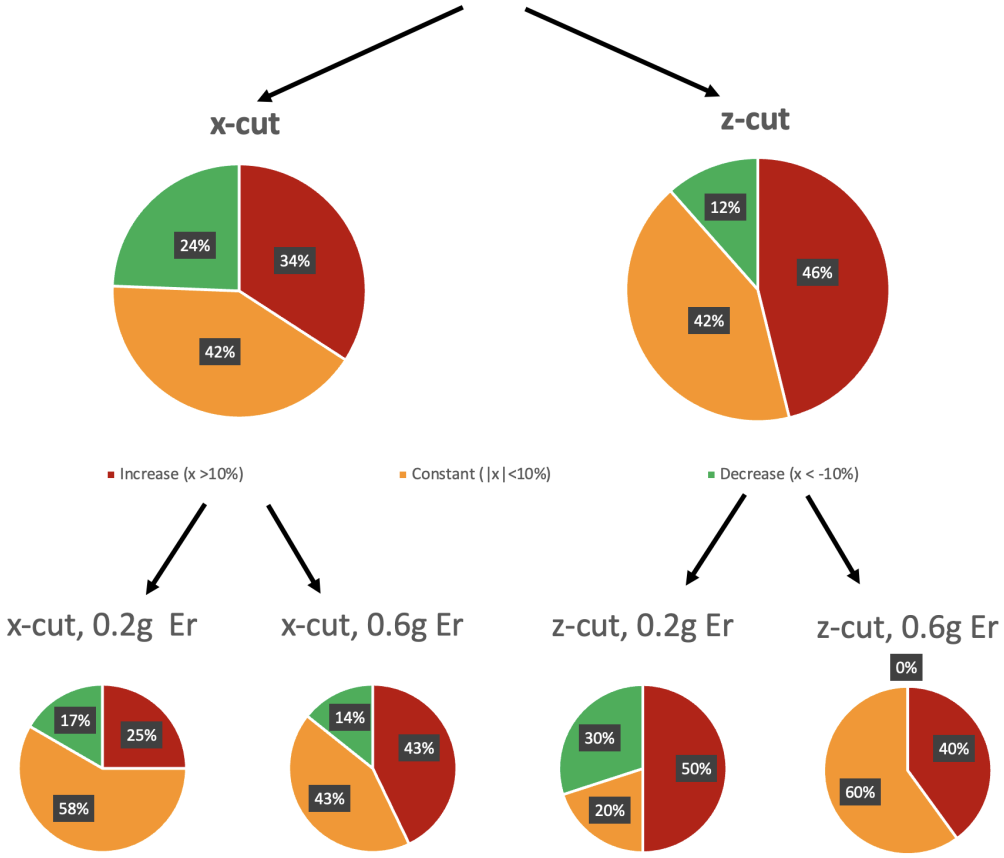

Figure 20: Determined possible Er diffusion chracterised according to doping concentration and crystal orientation of Er.

and

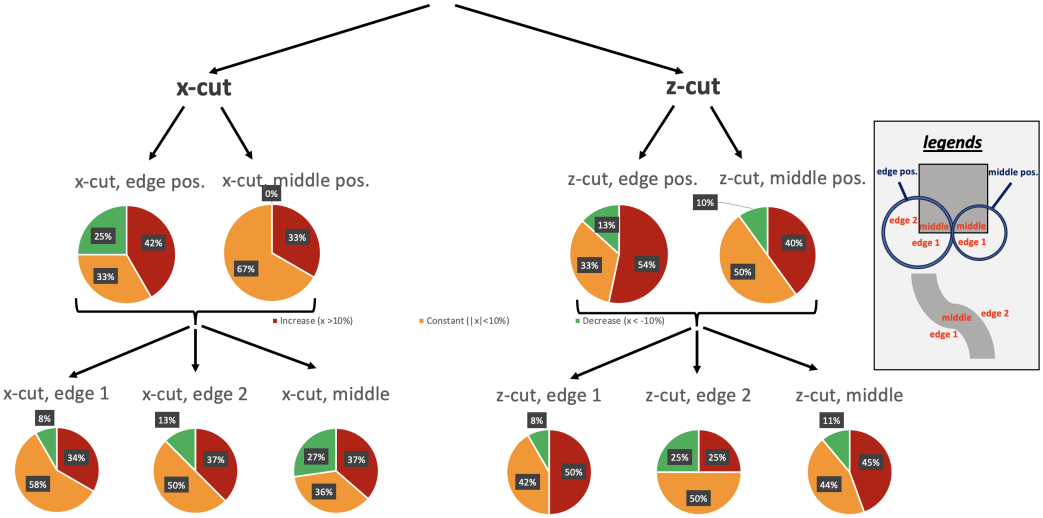

Figure 21: Determined possible Er diffusion chracterised according to position on chip.

Depth of Erbium Doping

An alternative hypothesis is that the Er is diffusing into the lower layers of the chip, thereby evading the EDS emloyed with the SEM. By applyig the Kanaya–Okayama model [85], the penetration depth of the SEM-PE can be estimated to be approximately 20 - 25 µm.

A second approach involved the use of the S/TEM instead of an SEM. Therefore a 10x10x1.0 µm section was cut out of the chip and again with FIB narrowed to a 10x10x0.10 µm piece. Then, a S/TEM was used to determine the elemental composition of the chip cross-section via EDS. This was conducted on different chips (x-cut-465-27:0.4, z-cut-465-27:0.4 and x-cut-465-27:1.0) according to crystal-orientation and Er-doping-concentration. The results, as illustrated in Figure 22, demonstrate that there was no diffusion of Er into the SiO_2 or even the Si layer. A deeper penetration of Er into the chip would have resulted in the formation of clear residues, which should have decreased in concentration with an increase in the downward gradient. It must be emphasised that Figure 22 gives the impression that Er is also present in deeper layers due to green dots. However, this is only background noise of the EDS colouring and quantitative EDS measurements confirm that 0.0 $\%_{atomic}$ of Er is present. Therefore, the hypothesis that Er diffuses deeper into the chips cannot be corroborated.

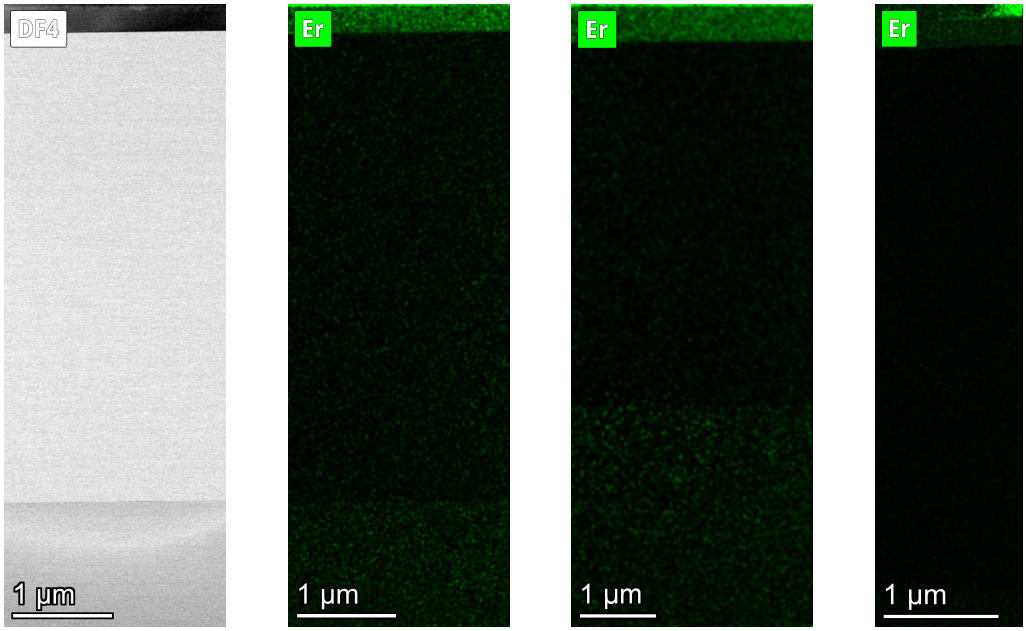

(a) (b) (c) (d)

Figure 22: FIB-S/TEM picture of Er-doped TFLN chip with clearly visible chip layers (a), EDS live tracking of Er atoms at various chips with visibly no Er (green) diffused into the SiO_2- or Si-layer for the chips x-cut-465-27:0.4 (a)+(b), z-cut-465-27:0.4 (c) and x-cut-465-27:1.0 (d).

In addition to the theoretical framework concerning the further diffusion of erbium, the EDS measurements illustrated in Figure 22 offer further confirmation that the diffusion of Er into the TFLN has been successful. It is encouraging to observe that the TFLN was also homogeneously doped, thereby demonstrating the effectiveness of the previously optimised doping recipe.

The following Figure 23 shows the live EDS tracking of further components of this. As Li cannot be detected by EDS, Nb represents LN. The image again highlights the layered cross-section of the chips used. It should be noted that these EDS measurements were taken before the chips were cleaned with a demineralised water bath, so K is still present on an in the TFLN.

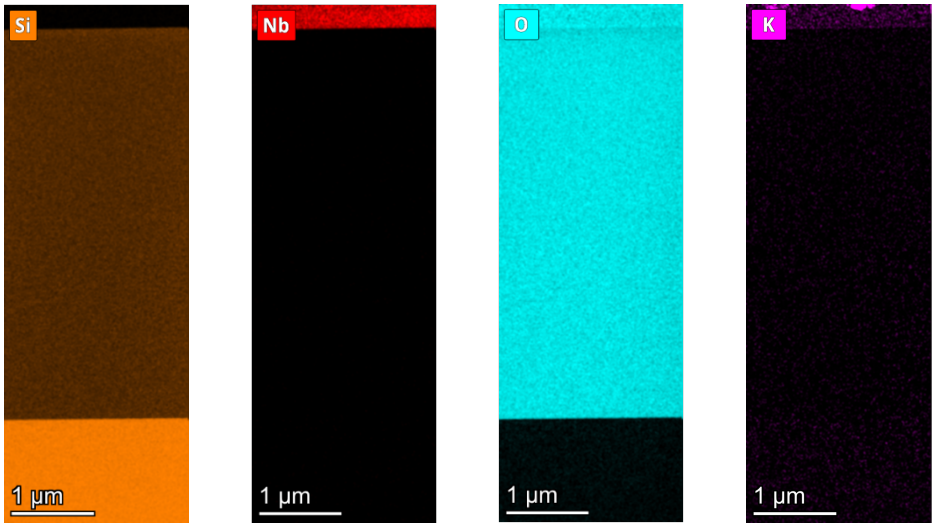

(a) (b) (c) (d)

Figure 23: Further elements detected by EDS on the chip from Figure 22.

Cleaning of the chips surfaces

A further crucial aspect of the doping process is the provision of a suitable chip for subsequent measurement series, which must be maintained alongside the doping. It is essential that the surface of the chips are sufficiently clean to permit the printing of the 3D couplers (as described in section 3.4.1) onto the predefined coupling areas (Figure 6). It is therefore essential to remove any dirt crystals originating from the doping process which may deposit and cover the coupling region or lay on top of the waveguide structures (Figure 24). Such crystals can decrease or even prevent transmission due to scattering, and thus must be completely removed from the surface. A summary of all cleaning attempts is provided in an overview table in Figures 33 and 34.

The initial cleaning procedures were conducted immediately following the annealing process, with the objective of preventing the further curing of the dirt crystals with air [86]. The dirt crystals were analysed using EDS measurements, which revealed that they include Er and K, which were assumed to be present in elementary form. The K crystals can be effectively removed by immersing the chips in a demineralised static water bath for 15 hours. However, the Er crystals remain untouched.

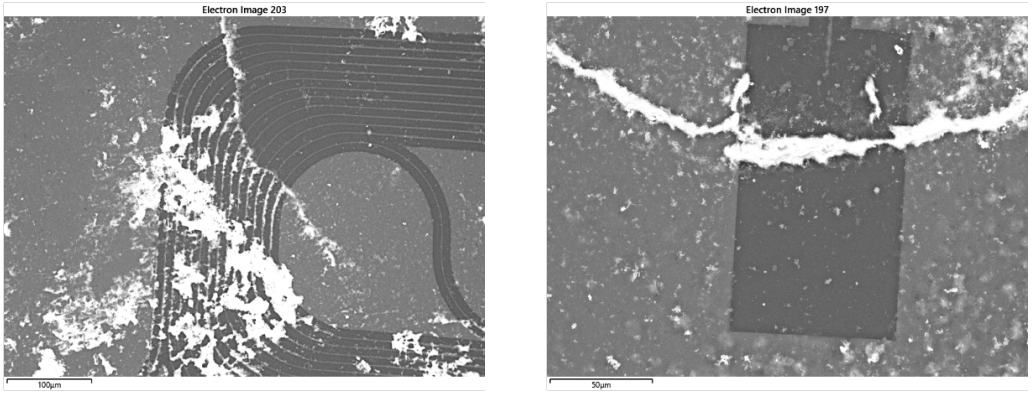

(a) (b)

Figure 24: Example for surface dirt covering the waveguide (a) and the coupling region (b)) on a x-cut-465-27:0.2 chip.

The intuitive cleaning method, which involved placing the chip in IPA or AC, sonicating it, and then rinsing it, proved to be ineffective. Consequently, the initial applied clenaing substances comprised conventional mixtures that are currently employed in the cleaning of photonic chips and waveguides. The first step involved the application of aqua regia (HNO_3 + 3 HCl) [87], which was employed to initiate the subsequent chemical reaction 4.1 [88]. It needs to be pointed out that the aggressiveness of aqua regia occurs not due to the acids HCL and HNO_3, but because of reaction products which arise when mixing the two acids. These products are nascent state Chlorine and (Cl_{nasc^-}) and Nitrosyl chloride (NOCl) [89]:

$$HNO_3 + 3\,HCl \rightarrow NOCl + Cl_{nasc^-} + 2\,H_2O \tag{4.1}$$

Especially Cl_{nasc^-} pushes Er to the third oxidation state making it a water-soluble chloride.
As impressively illustrated in Figure 25 the aqua regia effectively cleaned the surface, but it also dissolved all Er out of the TFLN. Probably, the Cl_{nasc^-} not only converted the surface Er but also the Er from the TFLN to Er-cloride compounds. This results in significant visible damage to the waveguide structure, so it can be concluded that aqua regia is unsuitable for the cleaning process in the present circumstances.

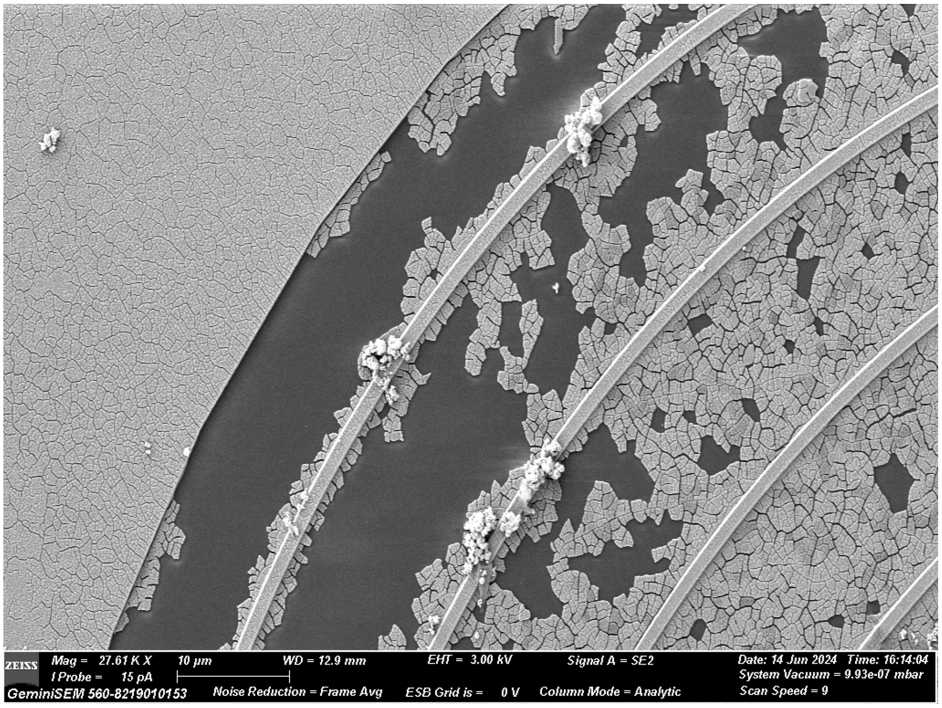

Figure 25: z-cut-465-27:0.2 chip after immersing for 1 min in aqua regia.

Next, the dirt was reconstructed to be probably not elementary Er, but an Er compound. Most probably, the Er oxidised via:

$$4\,\mathrm{Er(NO_3)_3} \rightarrow 2\,\mathrm{Er_2O_3} + 12\,\mathrm{NO_2} + 3\,\mathrm{O_2} \tag{4.2}$$

and formed erbium(III)-oxide (Er_2O_3) produced as residues from the previous doping phase, which involved the use KNO_3 and $Er(NO_3)_3$. Most likely, the K crystals removed with demineralised water were also potassium oxide (K_2O), which, however, has no detrimental effect on the solubility in water compared to K.

In the next cleaning attempt, the application of RCA 1 (hydrochloric acid, hydrogen peroxide and water, $HCl + H_2O_2 + 5\ H_2O$), a remover for organic residues and films from silicon wafers by sequentially oxidative desorption and complexing [90] is conducted for one minute. On this occasion, the TFLN sustained only minimal damage, but regrettably, the dirt crystals on top were also not removed to the extent that was required. The initiated following reaction was thus not efficient enough [91] [38].

$$\mathrm{Er_2O_3} + 6\,\mathrm{HCl} + 3\,\mathrm{H_2O_2} \rightarrow 2\,\mathrm{ErCl_3} + 3\,\mathrm{H_2O} + 3\,\mathrm{O_2} \tag{4.3}$$

Moreover, AR 60071, which is a medium for the removal of CSAR and other photoresists (comprising 1,3-Dioxolane and 1-Methoxy-2-propanol, 7 $C_3H_6O_2$ + 3 $C_4H_{10}O_2$ [92]), is applied for a period of 25 minutes.
Nevertheless, the desired outcome was not achieved. In comparison to the RCA-1, the damage to the TFLN was not as extensive, yet nevertheless significant, and the dirt crystals on the surface remained undisturbed. It may be postulated that instead of an attack on the dirt crystals, the AR 60071 engenders an Er-Complex of greater stability. This complex is formed with the participation of solvents, namely 1,3 Dioxolane and 1-Methoxy-2-propanol, which serve to stabilise the Er-ions.

As the preceding standardised photonic cleaning agents were found to be ineffective, the subsequent step was to utilise more specialised chemical compounds, designated as complexing agents. However, these and other subsequent series of measurements exceed the standard purification procedures of the working group. Subsequently, the following experiments were conducted at the Institute of Pharmacy and Molecular Biotechnology at the University of Heidelberg, in collaboration with the medicinal chemistry research group. The function of these chemical compounds is to enclose a metal, thereby forming a complex that is soluble in water, which can then be rinsed off.
The first compound used is Ethylenediaminetetraacetic acid (EDTA, $C_{10}H_{16}N_2O_8$), which is known for its ability to complex and dissolve ferrum (Fe)- and calcium (Ca)-containing substances even at neutral pH values, where their oxides are insoluble [93], is used. The initiated complex formation was most probably:

$$Er_2O_3 + 2\,Na_2H_2EDTA \rightarrow 2\,Na[Er(EDTA)] + Na_2O + 2\,H_2O \tag{4.4}$$

Na_2H_2EDTA represents the fully protonated form of EDTA, whereas Na[Er(EDTA)] denotes the Er-EDTA complex.
Despite the theoretical expectation of success, a 0.1 M[3] solution of EDTA with subsequent immersion in water was unable to clean the chip surfaces, even when the chip was immersed in EDTA for over 66 hours.

A second complex builder was employed in the form of sodium thiosulfate ($Na_2S_2O_3$), which functions in a similar manner to EDTA. The use of a 0.1 M solution resulted in the desired reaction:

$$Er_2O_3 + 6\,Na_2S_2O_3 + 6\,H_2O \rightarrow 2\,Na_3[Er(S_2O_3)_3] + 6\,NaOH + 3\,H_2O \tag{4.5}$$

[3]The term "1 M" is a "1-molar solution", which means that 1 litre of the solution contains 1 mol of a substance.

This approach proved to be effective. The initial formation of large crystals of dirt was reduced to small beads after 66 hours of immersion. It was observed that the application of hydrochloric acid (HCl) for a brief period was unable to eliminate the small beads, even when the immersion period was extended. However, the application of this method does result in a reduction of Er_2O_3-dirt on the chip surface by about 80%.

In order to create a comprehensive cleaning process, either in conjunction with or independent of sodium thiosulfate, a series of diverse acids with varying concentrations, durations and temperatures were employed in the subsequent measurement series. The specific parameter configuration can be found in Figures 33 and 34.

Initially, a number of acids were tested, but these were subsequently deemed unsuitable. On the one hand, there is 85 percent phosphoric acid (H_3PO_4), a low oxidising acid [56]. Its interaction with the Er_2O_3, most probably went the following during the two-minute reaction:

$$Er_2O_3 + 2\,H_3PO_4 \rightarrow 2\,ErPO_4 + 3\,H_2O \tag{4.6}$$

Not only all dirt crystals on the surface were removed, but also all Er in the TFLN. Thus, it might be a tray to use an higher oxidising acid, because then the oxidising strength, to lift the O_3^{-II} to O_2^0 is much higher. If this oxidisation process takes place efficently, simultaneously the Er^{III} get reduced to Er^0 and thus turn into a in water soluble substance.
Conversely, a highly oxidising 96 percent sulfuric acid (H_2SO_4) was applied over a period of up to 25 hours, triggering the reaction:

$$Er_2O_3 + 3\,H_2SO_4 \rightarrow 2\,Er_2\,(SO_4)_3 + 3\,H_2O \tag{4.7}$$

Here, all Er_2O_3 crystals were removed too. However, new crystals comprising Al, K and sodium (Na) emerged on the surface of the chips. But they origin most probable from the used demineralized water instead of ultra-pure water or from water residue from cleaning the pipette. In addition, the TFLN was severely damaged by small plates of TFLN coming loose and piling up at irregular intervals. .

Other acids demonstrated considerable promise. For instance, hydrochloric acid (HCl) proved highly effective at removing Er_2O_3 contamination as the immersion time was extended. At a sufficient level of cleaning, indicated by a surface purity, with 37 percent HCl and an immersion duration of 21 hours, not only were the Er_2O_3-crystals dissolved, but also the Er present

in the TFLN was removed. This outcome was attributed to the following reaction:

$$\mathrm{Er_2O_3 + 6\,HCl \rightarrow 2\,ErCl_3 + 3\,H_2O} \tag{4.8}$$

Another promising approach involved the use of either 100 percent acetic acid ($\mathrm{CH_3COOH}$) or 2 M citric acid ($\mathrm{HOCH_2C(COOH)C(OH)(CH_2COOH)COOH}$) for up to 64 hours each. In the majority of chips, the TFLN remained intact, the Er was not dissolved out of the TFLN, and the dirt crystals were almost entirely removed or reduced to a size of a few tens of nanometres. This value is equivalent to one-fifth of the original median particle size of the dirt crystals. Despite employing various techniques, including increasing the acid concentration, utilising a sonicator, and raising the temperature to extend the reaction time in accordance with the RGT rule [94], a comprehensive cleaning of the surface remained elusive. The reactions of the two acids, which effectively removed the majority of the dirt, were as follows:

$$\mathrm{Er_2O_3 + 6\,CH_3COOH \rightarrow 2\,Er(CH_3COOH)_3 + 3\,H_2O} \tag{4.9}$$

$$\begin{aligned}\mathrm{Er_2O_3 + 2\,HOCH_2C(COOH)C(OH)(CH_2COOH)COOH}\\ \mathrm{\rightarrow 2\,Er(HOCH_2C(COOH)(COO)(CH_2COO)) + 3\,H_2O}\end{aligned} \tag{4.10}$$

An alternative methodology for cleaning is to undertake this process prior to the annealing process, immediately following doping. This approach is designed to prevent the residues of $\mathrm{Er(NO_3)_3}$ from reacting to $\mathrm{Er_2O_3}$ via 4.2. The results demonstrated that the crystal structure of the Er-doped TFLN in this stadium is highly unstable. The application of hydrochloric, acetic or citric acid for brief periods of time (a few minutes) consistently resulted in the removal of all Er from the TFLN in all samples. Even the use of demineralised water proved not being purposeful. Manual swivelling for up to five minutes had no effect on the dirt or the Er in the TFLN. However, if one then switches to sonicating the chip, even after 2 seconds of sonication in demineralised water, all Er is dissolved out of the TFLN. This sensitive reaction of the TFLN crystal structure was unexpected, but serves to emphasise the importance of annealing after doping once again.

A third attempt at cleaning the surface was conducted by heating it to 100°C, while immersing it in ultra-pure water. By immersing the chips in ultra-pure water, the removal of the Er_2O_3 dirt should be initiated in an intermediate manner, driven by Brownian molecular motion rather than weak hand-shaking and intense sonication. It is anticipated that the simultaneous heating will facilitate a smooth annealing of the TFLN structure, thereby preventing the dissolution of the Er. Furthermore, the dissolution of the Er_2O_3 dirt crystals from the original 9 mm^2 chip now distributes over the 171-times larger area of the beaker when the ultra-pure water vaporises at 100°C. This should also result in a reduction in the number of dirt crystals on the chip surface.
It is regrettable to report that this method also proved unsuccessful. While the Er-ions remain within the TFLN structure, the crystal covering is reduced by only 20% after 6 h.

4.2 Reflection Measurements with Fiber-Coupled Setup

In the initial measurement series, distinct chips were illuminated with 980 nm or 1480 nm laser light with the objective of stimulating the transition from the $^4I_{11/2}$ to the $^4I_{13/2}$ and subsequently to the $^4I_{15/2}$ state, as outlined in section 2.3. Ultimately, the excitation of the $^4I_{11/2} \longrightarrow {}^4I_{13/2} \longrightarrow {}^4I_{15/2}$ (for 980 nm) and $^4I_{13/2} \longrightarrow {}^4I_{15/2}$ (for 1480 nm) transitions result in the emission of 1550 nm light via amplified spontaneous emission. The transmission of the employed components was initially validated through the application of a 1550 nm laser input with a power of (31.492 ± 0.005) mW, followed by the measurement of a 1550 nm reflection at the OSA with a power of (-42.70 ± 0.05) dBm (approximately (53.0 ± 1.0) nW. The chip utilised was of the z-cut-465-27:4.
Subsequently, the input laser was set to 1480 nm with an input power of 4.499 mW. An integration time of two minutes (equivalent to the internal Python setting "HIGH2") was used to record the Er spectrum at wavelengths of 1528–1534 nm and 1548–1552 nm. The chips employed were of the z-cut-465-27:4 and x-cut-465-27:0.4. It is unfortunate to report that no peaks were observed with the OSA during the course of the measurements. When the procedure was repeated with the same chips but with an input laser at 980 nm and an input power of (55.0 ± 2.0) mW, no detectable peaks were observed at 1550 nm or 1530 nm.
A second attempt was made to determine the OSA spectrum in the regions 1528 – 1534 nm and 1548 – 1552 nm once more, but this time in direct comparison with the background signal. This should guarantee the occurrence of a light emission by the chip, although it may not be perceptible due to

the presence of a much broader peak than was initially anticipated. The sample employed was a z-cut-465-27:4 chip. The CTL was employed as the input laser, with a wavelength of 980 nm and an input power of (50.0 ± 2.0) mW. The scanning time was set to the maximum sensitivity range from -90 dB to +20 dB, resulting in an integration time of approximately 25 minutes [95]. The results are presented in the following Figure, reference number 26. It can be observed that there is no discernible difference between the input laser being enabled or disabled.

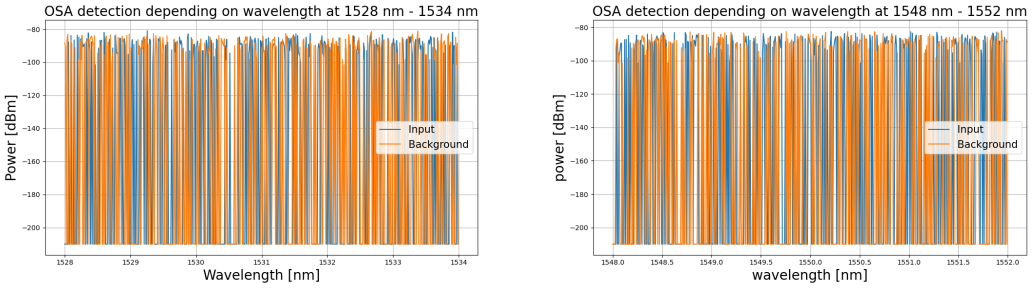

(a) (b)

Figure 26: (a) measurement of the ANDO OSA in an area of 1528 - 1534 nm with no expected peak at 1530.2 nm or difference in amplitude compared to the backgroudn signal, (b) repeated measurement at 1548 - 1552 nm with the same result.

This suggests a number of potential explanations. Firstly, it is possible that no excitation of the Er transition occurred, although this seems unlikely in light of the theoretical background. Secondly, it is possible that the transition was indeed excited, but that the emitted signal was too weak to be detected. In addition, the 1550 nm signal emitted by the chip may not be particularly weak, but its power is lost entirely along the path from the chip to the OSA, despite the use of specialised components designed for 1550 nm signals. However, the primary reason is likely to be insufficient input power of just milliwatts, which resulted in a negligible level of excitation that then got lost within the background. In order to enhance the input laser power, utilising the pulsed Mai Tai Laser as outlined in section 4.4 may prove an effective solution to this issue.

4.3 Measurements with Waveguide Transmission Setup

Subsequent to the alignment procedure delineated in section 3.4.1, a measurement series with waveguide chips to measure their transmission of optical power was prepared. Initially, the undoped x- and z-cut waveguide were employed as a reference for the subsequent doped TFLN waveguides. In order to facilitate a more meaningful comparison with the doped chips that would be produced subsequently, the undoped ones were also subjected to a heating process at 465°C for a period of four hours. Following this, they were annealed using the standard parameters of 200/300/400°C for 4/4/23 h.
For each chip and both CTL lasers, a calibration measurement is conducted by sweeping over the entire wavelength range.

Due to unforeseen technical issues with the printed 3D couplers, which were mentioned in section 13, it was unfortunately not possible to proceed with the planned transmission measurements. Further details on this matter can be found in the outlook 5.2.

4.4 Measurements with Free-Space Setup

The objective of the second setup was to detect 1550 nm light from the erbium atoms, given that the Mai Tai laser is capable of higher laser power, where the previously utilised CTL lasers were unable to achieve the desired outcome. Furthermore, it is anticipated that material-related losses in optical performance can be offset by the high power applied. The used Mai Tai laser emits thereby pulsed light on femtosecond scale, which cannot be resolved by the bandwidth of the power meter, resulting in the perception of the pulsed laser light as continuous. In general:

$$\mathrm{P}_{\text{peak-power}}\,[\mathrm{W}] = \frac{\mathrm{P}_{\text{average}}\,[\mathrm{W}]}{\text{Repetition rate}\,[\mathrm{Hz}] \cdot \text{Pulse width}\,[\mathrm{s}]} \tag{4.11}$$

With an average power output in the single-digit milliwatt range and a repetition rate of 8 MHz and a pulse width of 100 fs, the peak power rises rapidly to values in the high double-digit kilowatt range, which is 7 orders of magnitude higher than that observed input-power of 50 mW in the fibre-coupled configuration presented in section 4.2
In the following measurement series, the laser is pulsed with different powers onto the doped chip in order to gain various amounts of photon emission with a wavelength of 1550 nm. These photons were then supposed to be detected by the OSA.

It was not possible to achieve a 1550 nm emission correlated to the 980 nm input power measured by the OSA. The crucial issue was that, despite extensive optimisation and alignment efforts, it was not possible to couple the emitted 1550 nm light (if it was indeed emitted) from free space into the fibre as describes in Figure 14. It was imperative that all alignment procedures were conducted with either a visible 680 nm diode alignment laser or the MaiTai itself, operating at a wavelength of 980 nm.

Figure 27 illustrates the dependence of a shift in focal length due to the use of different wavelengths of a sample lens. The focal length of such a lens is dependent upon the refractive index of the lens material as a function of the wavelength and the radii of curvature of the lens surface. Lenses are usually manufactured with a correction for two wavelengths and a wavelength range with a smaller shift between these two. This ensures that the focal length in this range reacts less sensitively to the wavelength used with regard to a shift. If one considers that the final wavelength of 1550 nm is 850 nm away from the optimum at 700 nm and one assumes a linear regression, the focal length is already shifted by 2.1 mm by the two used telescope lenses. This was attempted to be rectified by mounting the second lens in the cage system in order to readjust by moving the lens within the system. However, if one also considers that the beam splitter, the galvometer and the objective in the galvometer are also only optimised for 980 nm and not 1550 nm light, the number of potential sources of error increases significantly. This is because, in addition to the focal length, the anti-reflective coating of the components is also ineffective outside the optimised area, so more reflections occur, reducing the singal-to-noise ratio (SNR) as well as the likleyhood of detecing upconverted light with a wavelength of 1550 nm.

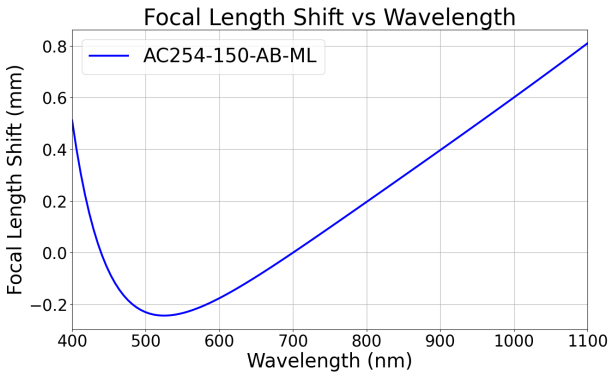

Figure 27: example dependece of focal length shift and wavelengh, data taken from [96].

This is how, for example during the construction of the telescope, three laser dots become visible on a laser card held into the beam path, indicating the inaccuracy in the setup. The smallest in diameter is reflective light from the chip, while the other two reflections originate from other components within

the cage system, most probably originating from the beam splitters. Moreover, the dots from the cage system components even exhibit an interference pattern. As the individual points are not far enough apart, it is unfortunately not possible to filter out individual points with pinholes.

In order to quantify the losses within the cage system, the power of the 980 nm input laser was measured with a free-space power meter at the positions 1-7 in Figure 14. Figure 28 illustrates the ideal course resulting from beam splitter losses, the actual course, and the background. It is evident that the actual course invariably exhibits greater losses. Nevertheless, the measurement indicates that these losses are so significant that at the crucial stage of coupling into the fibre for the OSA (measurement at point 7), the signal is indistinguishable from the background.

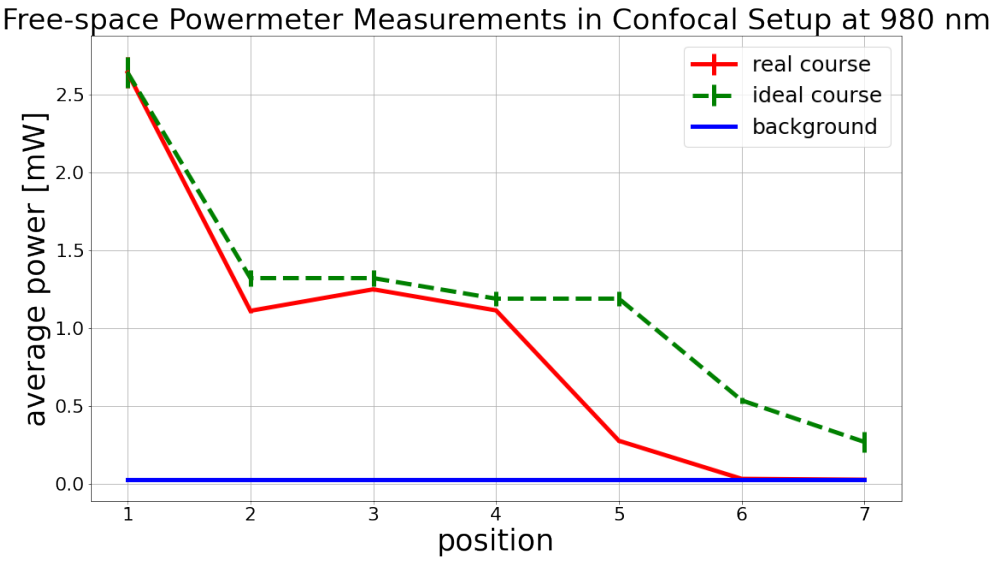

Figure 28: Free-space-powermeter measurements at different positions within the free-space with an input wavelength of 980 nm.

In order to anyway try to ascertain the relationship between the power of the detected 1550 nm signal and the 980 nm input power, a measurement series was taken with the free-space powermeter at position 5 in Figure 14. Measuring there is the first position in the cage system, where the input beam is seperated from the beam coming from the chip. Furthermore, the reflected chip-signal is not on background level so far as at position 6 or 7. The aver-

age power of the detected 1550 nm signal was found to indeed depend on the 980 nm input power. The subsequent Figure 29 (a) displays the individual values, the median value for each input power, and a fit function.

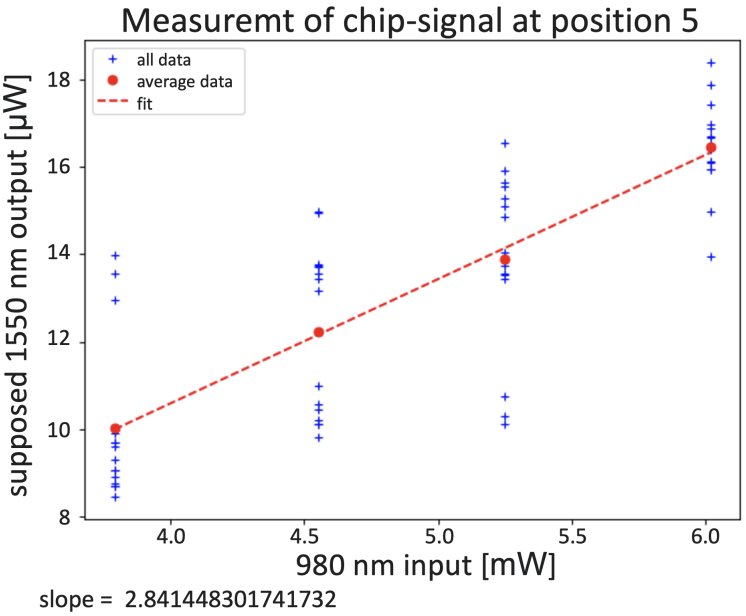

(a)

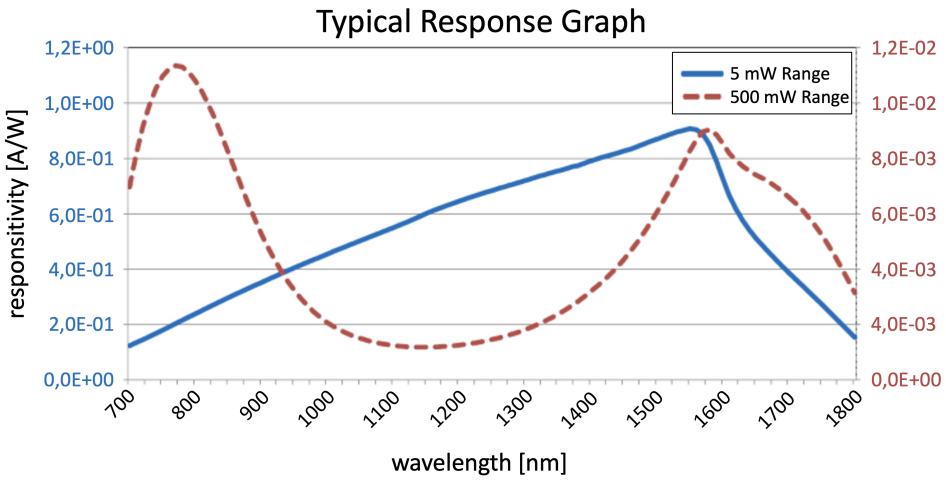

(b)

Figure 29: (a) measurement of supposedly 1550 nm light emitted by the chip, (b) Response graph of used free-space powermeter regarding different detected wavelengths. Taken changed from [96]

Nevertheless, the objective of quantifying 1550 nm radiation was promptly challenged again by the response graph of a free-space powermeter, as illustrated in Figure 29 (b). Although a free-space power meter is capable of measuring a range of wavelengths, it does not detect the individual wavelengths itself, as an OSA does. Instead of this, a distinct weighting factor is ascribed to each wavelength. An analysis of the graph reveals that a measurement of 1550 nm light would result in a slope of approximately 1 for the fitting curve. However, the observed slope in Figure 29 (a) is approximately 2.8, which corresponds to the reciprocal of the weighting factor in Figure 29 (b). It was thus established that the measured light at position e) was not 1550 nm emission from Er, but rather a reflection of the 980 nm input laser light.

5 Conclusion

In the following, the preceding work about the Er-doping is summarised, and an outlook on the subsequent stages of the project are presented.

5.1 Summary

The objective of this bachelor thesis is to develop a localized doping method for LN waveguides with Er to compensate for optical signal losses in photonic chips. Unlike global doping methods currently available, this approach aims to enhance specific regions of the chip. Theoretical foundations covered the material properties of LN and Er, and the optical amplification achievable through Er's stimulated emission.
Through continuous monitoring using SEM and EDS, optimal doping parameters were established based on low-temperature ion diffusion. The primary goal was to maximize Er incorporation without causing structural damage such as cracking or flaking. The process involves heating a chip, cleaned with AC and IPA, at temperature increase of 30°C/min in a salt mixture of 27 g KNO_3 and 0.6 g $Er(NO_3)_3$ to 465°C for 4 hours. For structured chips, the Er amount is reduced to 0.4g due to a 66% increase in doping surface area. Post-doping, the chips undergo annealing at 200°C, 300°C, and 400°C with $\Delta T = 20°C/h$ for 4h, 4h, and 23h respectively.

All measurements were conducted in parallel on x- and z-cut chips, ensuring that the optimal parameters are equally applicable to both chip types. As illustrated in Figure 30 on the right-hand side, the results were successful. The Er diffused homogenously into the TFLN layer, without penetrating into the deeper layers of the chip. Doping results in Er_2O_3 and K_2O contaminants on the chip surfaces, which require removal. K_2O can be dissolved in distilled water, while various acids, acid mixtures, and complexing agents were tested for Er_2O_3 removal. Sodium thiosulfate proved most effective, removing over 80% of Er_2O_3 without damaging the TFLN or leaching out

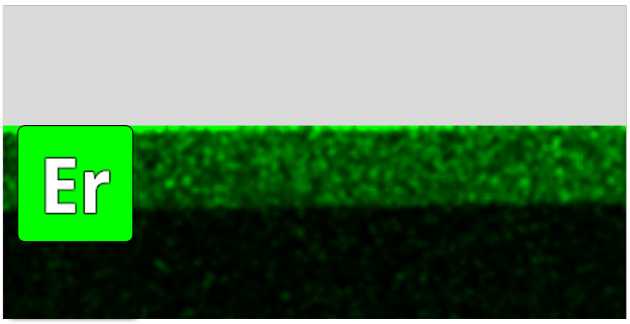

Figure 30: Live-tracking of Er in the TFLN layer with EDS (zoomed in).

diffused Er. Despite this, even minimal surface contamination can obstruct waveguide transmission, necessitating complete cleaning.
The parameters just listed for performing the low temperature ion exchange method provide a solid basis for future doping of LN with Er. But for these, the durability of the chip and constant Er concentration in the TFLN play a central role. Given that doping was conducted via low-temperature ion diffusion, concerns arose that even room temperature could precipitate further diffusion of Er within the TFLN. To test this hypothesis, two series of measurements were conducted.
Despite various experiments and hypotheses that the Er could diffuse alongside the tunnel structures in the LN-crystal or even down into deeper layers of the chip, non of these concerns could be confirmed, which is very promising for future applications.
Although the cleaning of the chip surface has made good progress with 100% removal of K_2O crystals and over 80 % removal of Er_2O_3 crystals, it is relevant for efficient use in telecommunication, as motivated in the introduction, that there are as few scattering possibilities as possible for propagating light in the LN. However, every dirty crystal forms such a scattering centre and at the same time prevents the printing of the 3D couplers required for transmission measurements. It is also surprising that despite excessive duration and concentration, no further reduction in the size of the dirt crystals took place after a certain point. In the further course of the project, even greater co-operation should be sought with chemists in order to clean the chip surfaces as completely as possible.
Furthermore, the material conditions for many measurement series were not yet optimal during this work. It was almost to be expected that the power of the TOPTICA laser in section 4.2 would not be sufficient to detect measurable spontaneous amplified emission of erbium with the OSA. However, the subsequent series of measurements using the pulsed free-beam optical Mai Tai laser was also unable to produce the desired spontaneous light emission of Er. The losses in the cage system were still too great due to components such as lenses or beam splitters that were not optimised for the far-infrared wavelength. However, it is to be expected that the series of measurements with optimised components would lead to success. It was a great pity that for logistical reasons it was no longer possible to print 3D couplers as part of this work. The transmission measurements carried out with them using undoped waveguides would have provided a basis of comparative values for later transmission measurements with doped waveguides.

Apart from these few shortcomings, the results of this work provide a good starting point for the further development process of locally doping LN.

5.2 Outlook

The next approach to continue the previous project is to further clean the surfaces of the waveguide chips. Another approach would be to develop a mechanical-chemical polishing process to smooth the chip surfaces. It would have to be tested whether this is possible without damaging the structure of the LN. In parallel, however, transmission measurements using doped waveguides could also be started. This would show whether 100 per cent surface cleaning is necessary at all or whether, contrary to expectations, smaller residues are unproblematic.
Furthermore, the transmission measurements will most likely also be used to adjust the amount of Er during the doping process. This is because it is important to note that every Er atom in the TFLN represents a potential scattering centre for signals, particularly due to its size. This means that the maximum amount of Er that can diffuse into the TFLN, whether or not its surface is occupied, may not also mean maximum amplification.

By covering those areas on a waveguide with a mask, e.g. made of SiO_2, during the doping process in a further step, any locally limited window can then be selected from the previous global doping of a waveguide in a final step. If this masking is also optimised, a successful method will be available with which LN can be doped locally with Er. This process can then be used for telecommunications processes that are to be optimised using the unique material lithium niobate.

6 References

List of Figures

List of abbreviations

LN	lithium niobate, $LiNbO_3$
TFLN	Thin-film nithium niobate
Al	aluminium
Ar	argon
Ca	calcium
C	carbon
Er	Erbium
Fe	ferrum
He	helium
H	hydrogen
Li	lithium
Nb	niobium
N	nitrogen
O	oxygen
K	potassium
Si	silicon

Na	sodium
AC	aceton, CH_3COCH_3
$Er(NO_3)_3$	erbium(III) nitrate pentahydrate
Er_2O_3	erbium(III)-oxide
InP	indium phosphide
IPA	isopropyl alcohol, $CH_3CHOHCH_3$
KNO_3	potassium nitrate
K_2O	potassium oxide
SiO_2	silicon dioxide
Si_3N4	silicon nitride
WDM	Wavelength Division Multiplexing
ITU-T	Comité Consultatif International Télégraphique et Téléphonique
O	original band
E	extended band
S	short wavelength band
C	conventional band
L	long wavelength band
U	ultralong wavelength band
AFM	Atomic Force Microscopy
BSE	Backscattering Electrons
DWDM	Dense Wavelength Divison Multiplexing
EBPL	Electron Beam Pattering Lithography
EDS	Energy Dispersive X-ray Spectroscopy
EDFA	Erbium Doped Fiber Amplier

ET	Everhart-Thorlay detector
FET	Field-Effect-Transistor
FIB	Focused Ion Beam
FWHM	Full Width at Half Maximum
GUI	Graphical User Interface
ICP-RIE	Inductively Coupled Plasma Etching
MCA	Multichannel Analyzer
OM	Optical Microscopy
OSA	Optical Spectrum Analyzer
PE	Primary Electrons
SEM	Scanning Electron Microscopy
S/TEM	Scanning Transmission Electron Microscope
SE	Secondary Electrons

6.1 Acknowledgement

At this point, I want to express my sincere gratitude to Prof. Wolfram Pernice for giving me the opportunity to work in his research group for my thesis and get acquainted with integrated photonics and to Prof. Lauriane Chomaz for agreeing to be the second examiner for this thesis.

I would also like to thank Rasmus Bankwitz for supervising my work, his personal care and his professional guidance at every step during this thesis, including the final revision.

I am very thankful for Dr. Shabnam Taheriniya, Dr. Xinyu Ma, Dominik Ditz, Marc Ulanov, Julius Römer and Philipp Lohmann sharing their knowledge and years of experience with all the setups I used and for proofreading my thesis.

Furthermore, I want to thank Raphael Berger, Judith Stirn, Dominik Mytzka and Robin Kugler from the Medical Chemistry Group of the Institute of Pharmacy and Molecular Biotechnology and Maximilian Kaiser from the Jochim Labs at Institute of Physics for their interdisciplinary advices and providing of specilized infrastructure.

Finally, I thank all members of my group Neuromorphic Quantumphotonics at the Kirchhoff Institute for Physics for their professional input in the group meetings and for their emotional support.

Erklärung

Ich versichere, dass ich diese Arbeit selbstständig verfasst und keine anderen als die angegebenen Quellen und Hilfsmittel benutzt habe. Zur Überprüfung der englischen Rechtschreibung dieser Arbeit wurden Deepl und ChatGPT verwendet.

Heidelberg, den 09.08.2024,

Michael Uwe Gotzmann

References

[1] *Cisco Annual Internet Report - Cisco Annual Internet Report (2018–2023) White Paper*. https://www.cisco.com/c/en/us/solutions/collateral/executive-perspectives/annual-internet-report/white-paper-c11-741490.html. (Visited on 08/07/2024).

[2] Alan Mauldin. *Do Submarine Cables Account For Over 99% of Intercontinental Data Traffic?* https://blog.telegeography.com/2023-mythbusting-part-3. (Visited on 08/07/2024).

[3] Gerd Keiser. *Optical Fiber Communications*. 4. ed. Literaturangaben. New York, NY: McGraw-Hill, 2011. ISBN: 978-0-07-338071-1.

[4] G. P. Agrawal. *Fiber-Optic Communication Systems*. 3rd ed. Wiley Series in Microwave and Optical Engineering. "A Wiley-Interscience publication.". New York: Wiley-Interscience, 2002. ISBN: 978-0-471-21571-4.

[5] James E. Toney. *Lithium Niobate Photonics*. Artech House Applied Photonics Library. Literaturverzeichnis Seite: 258-259. Boston London: Artech House, 2015. ISBN: 978-1-60807-923-0.

[6] Juan-Jose Crespo, José L. Sánchez, and Francisco J. Alfaro-Cortés. "Silicon Photonic Networks: Signal Loss and Power Challenges". In: *Concurrency and Computation: Practice and Experience* 31.21 (Nov. 2019), e4777. ISSN: 1532-0626, 1532-0634. DOI: 10.1002/cpe.4777. (Visited on 08/07/2024).

[7] David A. B. Miller. “Meshing Optics with Applications”. In: *Nature Photonics* 11.7 (July 2017), pp. 403–404. ISSN: 1749-4893. DOI: 10.1038/nphoton.2017.104. (Visited on 07/11/2024).

[8] Richard Soref. “The Past, Present, and Future of Silicon Photonics”. In: *IEEE Journal of Selected Topics in Quantum Electronics* 12.6 (Nov. 2006), pp. 1678–1687. ISSN: 1558-4542. DOI: 10.1109/JSTQE.2006.883151. (Visited on 07/11/2024).

[9] Mohammadreza Younesi et al. “Erbium Doping of Lithium Niobate on Insulator Using Low-Temperature Ion Exchange”. In: *Optical Materials Express* 14.1 (Jan. 2024), p. 157. ISSN: 2159-3930. DOI: 10.1364/OME.500099. (Visited on 06/07/2024).

[10] American Elements. *Erbium-Doped Lithium Niobate*. https://www.americanelements.com/erbium-doped-lithium-niobate . (Visited on 07/11/2024).

[11] M. Mattarelli et al. “Characterization of Erbium Doped Lithium Niobate Crystals and Waveguides”. In: *Optical Materials* 28.11 (Aug. 2006), pp. 1292–1295. ISSN: 09253467. DOI: 10.1016/j.optmat.2006.01.030. (Visited on 07/11/2024).

[12] Nune Mkhitaryan et al. “Electro-Optic Properties of Singly and Doubly Doped Lithium Niobate Crystal by Rare Earth Elements for Optoelectronic and Laser Applications”. In: *The European Physical Journal Applied Physics* 85.3 (Mar. 2019), p. 30502. ISSN: 1286-0042, 1286-0050. DOI: 10.1051/epjap/2019180317. (Visited on 07/11/2024).

[13] *Ion-Exchange in Glasses and Crystals: From Theory to Applications*. MDPI, Sept. 2021. ISBN: 978-3-0365-1900-5 978-3-0365-1901-2. DOI: 10.3390/books978-3-0365-1900-5. (Visited on 08/07/2024).

[14] Aviad Katiyi and Alina Karabchevsky. “Passive and Active Materials for Advanced Photonic Integrated Circuitry in Visible and Near-Infrared”. In: *Encyclopedia of Materials: Electronics*. Elsevier, 2023, pp. 193–202. ISBN: 978-0-12-819735-6. DOI: 10.1016/B978-0-12-819728-8.00012-7. (Visited on 07/16/2024).

[15] Mitesh Vegad and N.M. Bhatt. “Review of Some Aspects of Single Crystal Growth Using Czochralski Crystal Growth Technique”. In: *Procedia Technology* 14 (2014), pp. 438–446. ISSN: 22120173. DOI: 10.1016/j.protcy.2014.08.056. (Visited on 07/16/2024).

[16] R. S. Weis and T. K. Gaylord. "Lithium Niobate: Summary of Physical Properties and Crystal Structure". In: *Applied Physics A Solids and Surfaces* 37.4 (Aug. 1985), pp. 191–203. ISSN: 0721-7250, 1432-0630. DOI: 10.1007/BF00614817. (Visited on 06/07/2024).

[17] Donald Sands. *Introduction to Crystallography*. Dover Classics of Science and Mathematics. Originally published: Reading, Mass. : W.A. Benjamin, 1969 (corrected printing 1975) (Physical chemistry monograph series). New York: Dover, 1993. ISBN: 978-0-486-67839-9.

[18] Pietro Ferraro, Simonetta Grilli, and Paolo De Natale, eds. *Ferroelectric Crystals for Photonic Applications: Including Nanoscale Fabrication and Characterization Techniques*. Vol. 91. Springer Series in Materials Science. Berlin, Heidelberg: Springer Berlin Heidelberg, 2014. ISBN: 978-3-642-41085-7 978-3-642-41086-4. DOI: 10.1007/978-3-642-41086-4. (Visited on 07/05/2024).

[19] Di Zhu et al. "Integrated Photonics on Thin-Film Lithium Niobate". In: *Advances in Optics and Photonics* 13.2 (June 2021), p. 242. ISSN: 1943-8206. DOI: 10.1364/AOP.411024. (Visited on 06/07/2024).

[20] Junxia Zhou et al. "On-Chip Integrated Waveguide Amplifiers on Erbium-Doped Thin-Film Lithium Niobate on Insulator". In: *Laser & Photonics Reviews* 15.8 (Aug. 2021), p. 2100030. ISSN: 1863-8880, 1863-8899. DOI: 10.1002/lpor.202100030. (Visited on 06/07/2024).

[21] *DDOC_T_2019_0256_DANIELYAN.Pdf*. http://docnum.univ-lorraine.fr/public/DDOC_T_2019_0256_DANIELYAN.pdf. (Visited on 07/17/2024).

[22] Mohammad Amin Baghban. *Integrated Nanophotonic Devices in Lithium Niobate*. KTH Royal Institute of Technology, 2018. ISBN: 978-91-7729-977-6.

[23] Yanne K. Chembo. "Kerr Optical Frequency Combs: Theory, Applications and Perspectives". In: *Nanophotonics* 5.2 (June 2016), pp. 214–230. ISSN: 2192-8614. DOI: 10.1515/nanoph-2016-0013. (Visited on 07/16/2024).

[24] A. R. Zanatta. "The Optical Bandgap of Lithium Niobate (LiNbO3) and Its Dependence with Temperature". In: *Results in Physics* 39 (Aug. 2022), p. 105736. ISSN: 2211-3797. DOI: 10.1016/j.rinp.2022.105736. (Visited on 07/18/2024).

[25] Amirhassan Shams-Ansari et al. "Reduced Material Loss in Thin-Film Lithium Niobate Waveguides". In: *APL Photonics* 7.8 (Aug. 2022), p. 081301. ISSN: 2378-0967. DOI: 10.1063/5.0095146. (Visited on 08/03/2024).

[26] Bich-Yen Nguyen, George Celler, and Carlos Mazuré. "A Review of SOI Technology and Its Applications". In: *Journal of Integrated Circuits and Systems* 4.2 (2009), pp. 51–54. ISSN: 1872-0234. DOI: 10.29292/jics.v4i2.297. (Visited on 07/12/2024).

[27] M. Levy et al. "Fabrication of Single-Crystal Lithium Niobate Films by Crystal Ion Slicing". In: *Applied Physics Letters* 73.16 (Oct. 1998), pp. 2293–2295. ISSN: 0003-6951, 1077-3118. DOI: 10.1063/1.121801. (Visited on 07/05/2024).

[28] Zhenlin Wu et al. "Investigation of High-Q Lithium Niobate-Based Double Ring Resonator Used in RF Signal Modulation". In: *Applied Sciences* 13.7 (Apr. 2023), p. 4648. ISSN: 2076-3417. DOI: 10.3390/app13074648. (Visited on 07/05/2024).

[29] Cheng Wang et al. "Integrated Lithium Niobate Electro-Optic Modulators Operating at CMOS-compatible Voltages". In: *Nature* 562.7725 (Oct. 2018), pp. 101–104. ISSN: 1476-4687. DOI: 10.1038/s41586-018-0551-y. (Visited on 07/05/2024).

[30] Mian Zhang et al. "Broadband Electro-Optic Frequency Comb Generation in a Lithium Niobate Microring Resonator". In: *Nature* 568.7752 (Apr. 2019), pp. 373–377. ISSN: 1476-4687. DOI: 10.1038/s41586-019-1008-7. (Visited on 07/05/2024).

[31] Jia-yang Chen et al. "Efficient Parametric Frequency Conversion in Lithium Niobate Nanophotonic Chips". In: *OSA Continuum* 2.10 (Oct. 2019), pp. 2914–2924. ISSN: 2578-7519. DOI: 10.1364/OSAC.2.002914. (Visited on 07/05/2024).

[32] Cheng Wang et al. "Ultrahigh-Efficiency Wavelength Conversion in Nanophotonic Periodically Poled Lithium Niobate Waveguides". In: *Optica* 5.11 (Nov. 2018), pp. 1438–1441. ISSN: 2334-2536. DOI: 10.1364/OPTICA.5.001438. (Visited on 07/05/2024).

[33] Wei C. Jiang and Qiang Lin. "Chip-Scale Cavity Optomechanics in Lithium Niobate". In: *Scientific Reports* 6.1 (Nov. 2016), p. 36920. ISSN: 2045-2322. DOI: 10.1038/srep36920. (Visited on 07/05/2024).

[34] Alessandro Prencipe, Mohammad Amin Baghban, and Katia Gallo. "Tunable Ultranarrowband Grating Filters in Thin-Film Lithium Niobate". In: *ACS Photonics* 8.10 (Oct. 2021), pp. 2923–2930. DOI: 10.1021/acsphotonics.1c00383. (Visited on 07/05/2024).

[35] R. Dixon. "Acoustic Diffraction of Light in Anisotropic Media". In: *IEEE Journal of Quantum Electronics* 3.2 (Feb. 1967), pp. 85–93. ISSN: 1558-1713. DOI: 10.1109/JQE.1967.1074447. (Visited on 07/05/2024).

[36] S. E. Harris and R. W. Wallace. “Acousto-Optic Tunable Filter*”. In: *JOSA* 59.6 (June 1969), pp. 744–747. DOI: 10.1364/JOSA.59.000744. (Visited on 07/05/2024).

[37] I. P. Kaminow and E. H. Turner. “Electrooptic Light Modulators”. In: *Applied Optics* 5.10 (Oct. 1966), p. 1612. ISSN: 0003-6935, 1539-4522. DOI: 10.1364/AO.5.001612. (Visited on 07/05/2024).

[38] Pradyot Patnaik. *Handbook of Inorganic Chemicals*. McGraw-Hill Handbooks. New York: McGraw-Hill, 2003. ISBN: 978-0-07-049439-8.

[39] John Emsley. *Nature’s Building Blocks: An A-Z Guide to the Elements*. Reprinted with corrections. Originally published: 2001. Oxford: Oxford Univ. Press, 2003. ISBN: 978-0-19-850340-8.

[40] Powell Spedding F. H. J. E. “Early Paper on the Use of Displacement Ion-Exchange Chromatography to Separate Rare Earths:” in: *Chemical Engineering Progress* 50 (1954), pp. 7–15.

[41] K. Iga. “Surface-Emitting Laser-Its Birth and Generation of New Optoelectronics Field”. In: *IEEE Journal of Selected Topics in Quantum Electronics* 6.6 (Nov. 2000), pp. 1201–1215. ISSN: 1077-260X, 1558-4542. DOI: 10.1109/2944.902168. (Visited on 07/15/2024).

[42] HYC Co Ltd. *What Is C Band and L Band in WDM (Wavelength Division Multiplexing)?* July 2020. (Visited on 07/15/2024).

[43] “RECOMMENDATION ITU-R V.431-8 - Nomenclature of the Frequency and Wavelength Bands Used in Telecommunications”. In: ().

[44] *Stimulated Emission - an Overview — ScienceDirect Topics*. https://www.sciencedirect.com/topics/physics-and-astronomy/stimulated-emission. (Visited on 07/31/2024).

[45] Christophe.Finot. *Niveaux d’énergie*. June 2006.

[46] Dr Rüdiger Paschotta. *Erbium-Doped Laser Gain Media*. https://www.rp-photonics.com/erbium_doped_laser_gain_media.html . (Visited on 06/09/2024).

[47] . *980/1480 Nm Pump Wavelength Used in EDFA Amplifier , DWDM Fiber — ROADM — OTN #roadm #otn*. YouTube Video. 2022.

[48] Minglu Cai et al. “Erbium-Doped Lithium Niobate Thin Film Waveguide Amplifier With 16 dB Internal Net Gain”. In: *IEEE Journal of Selected Topics in Quantum Electronics* 28.3 (May 2022), pp. 1–8. ISSN: 1077-260X, 1558-4542. DOI: 10.1109/JSTQE.2021.3137192. (Visited on 06/07/2024).

[49] Danny G O'Shea et al. "All Taper Coupled Microspherical Light Source". In: ().

[50] Zhiwei Fang et al. "An Erbium-Doped Waveguide Amplifier on Thin Film Lithium Niobate with an Output Power Exceeding 100 mW". In: ().

[51] Jiangwei Wu et al. "Efficient Integrated Amplifier-Assisted Laser on Erbium-Doped Lithium Niobate". In: *ACS Photonics* 11.5 (May 2024), pp. 2114–2122. ISSN: 2330-4022, 2330-4022. DOI: 10.1021/acsphotonics.4c00391. (Visited on 06/07/2024).

[52] Klaus Hentschel. "Stark Effect". In: *Compendium of Quantum Physics*. Ed. by Daniel Greenberger, Klaus Hentschel, and Friedel Weinert. Berlin, Heidelberg: Springer Berlin Heidelberg, 2009, pp. 738–742. ISBN: 978-3-540-70622-9 978-3-540-70626-7. DOI: 10.1007/978-3-540-70626-7_209. (Visited on 07/16/2024).

[53] *Zeeman Effect - an Overview — ScienceDirect Topics*. https://www.sciencedirect.com/topics/chemistry/zeeman-effect. (Visited on 07/16/2024).

[54] *Erbium.Png 3.880×1.292 Pixels*. https://upload.wikimedia.org/wikipedia/commons/7/7b/Erbium.png. (Visited on 06/27/2024).

[55] *Er(NO3)3.5H2O.Pdf*. https://www.ltschem.com/msds/Er(NO3)3.5H2O.pdf. (Visited on 07/27/2024).

[56] . *CRC Handbook of Chemistry and Physics*. 86TH Edition. Vol. FL 2005. CRC Press, Taylor & Francis, Boca Raton, 2005/2006.

[57] J. E. Macintyre and Chapman and Hall, eds. *Dictionary of Inorganic Compounds*. 1st ed. Updated by supplements
v. 1. Ac-C_{10} – v. 2. C_{11}-C_{45} – v. 3. C_{46}-Zr – v. 4. Structural type index, name index, CAS registry number index – v. 5. Element index. London ; New York: Chapman & Hall, 1992. ISBN: 978-0-412-30120-9.

[58] A. Einstein. "Über Die von Der Molekularkinetischen Theorie Der Wärme Geforderte Bewegung von in Ruhenden Flüssigkeiten Suspendierten Teilchen". In: *Annalen der Physik* 322.8 (Jan. 1905), pp. 549–560. ISSN: 0003-3804, 1521-3889. DOI: 10.1002/andp.19053220806. (Visited on 07/10/2024).

[59] *Welcome to the Gdshelpers' Documentation! — Gdshelpers 1.2.1 Documentation*. https://gdshelpers.readthedocs.io/en/latest/. (Visited on 06/18/2024).

[60] Helge Gehring et al. “Python Based Open Source Design Framework for Integrated Nanophotonic and Superconducting Circuitry with 2D-3D-hybrid Integration”. In: *OSA Continuum* 2.11 (Nov. 2019), pp. 3091–3101. ISSN: 2578-7519. DOI: 10.1364/OSAC.2.003091. (Visited on 06/18/2024).

[61] J. Rasmus Bankwitz et al. “Towards “Smart Transceivers” in FPGA-controlled Lithium-Niobate-on-Insulator Integrated Circuits for Edge Computing Applications [Invited]”. In: *Optical Materials Express* 13.12 (Dec. 2023), pp. 3667–3676. ISSN: 2159-3930. DOI: 10.1364/OME.503340. (Visited on 06/28/2024).

[62] Fabian Kaufmann et al. “Redeposition-Free Inductively-Coupled Plasma Etching of Lithium Niobate for Integrated Photonics”. In: *Nanophotonics* 12.8 (Apr. 2023), pp. 1601–1611. ISSN: 2192-8614. DOI: 10.1515/nanoph-2022-0676. (Visited on 07/03/2024).

[63] A. Säynätjoki et al. “Angled Sidewalls in Silicon Slot Waveguides: Conformal Filling and Mode Properties”. In: *Optics Express* 17.23 (Nov. 2009), pp. 21066–21076. ISSN: 1094-4087. DOI: 10.1364/OE.17.021066. (Visited on 07/20/2024).

[64] Ravi Rao. *Atomic Force Microscopy Explained: Principles, Construction, Working, and Applications*. https://www.wevolver.com/article/atomic-force-microscopy-explained-principles-construction-working-and-applications, https://www.wevolver.com/article/atomic-force-microscopy-explained-principles-construction-working-and-applications. (Visited on 06/09/2024).

[65] *Ultim Max - Nanoanalysis*. https://nano.oxinst.com/products/ultim-max. (Visited on 07/30/2024).

[66] Hitachi High-Tech in UK. *Ultra-High Resolution Scanning Electron Microscope SU9000II*. https://www.hitachi-hightech.com/uk/en/products/microscopes/sem-tem-stem/fe-sem/su9000.html. (Visited on 06/09/2024).

[67] Azad Mohammed and Avin Abdullah. “Scanning Electron Microscopy (SEM): A Review”. In: ().

[68] T. E. Everhart and R. F. M. Thornley. “Wide-Band Detector for Micro-Microampere Low-Energy Electron Currents”. In: *Journal of Scientific Instruments* 37 (July 1960), pp. 246–248. ISSN: 0950-1290. DOI: 10.1088/0950-7671/37/7/307. (Visited on 06/09/2024).

[69] Erik Luyk. *Backscattered Electrons in SEM Imaging*. https://www.thermofisher.com/blog/materials/backscattered-electrons-in-sem-imaging/. Dec. 2019. (Visited on 06/09/2024).

[70] Tushar Rukari and Alhat Babita. "Review Article TRANSMISSION ELECTRON MICROSCOPY-AN OVERVIEW". In: 1 (Aug. 2013), pp. 1–7.

[71] David B. Williams and C. Barry Carter. *Transmission Electron Microscopy*. Boston, MA: Springer US, 2009. ISBN: 978-0-387-76500-6 978-0-387-76501-3. DOI: 10.1007/978-0-387-76501-3. (Visited on 07/30/2024).

[72] *Prep-Fib-Samples.Pdf*. https://protochips.com/wp-content/uploads/2017/10/prep-fib-samples.pdf. (Visited on 07/02/2024).

[73] *Energy-Dispersive X-ray Spectroscopy (EDS)*. https://chem.libretexts.org/Courses/Franklin_and_Marshall_College/Introduction_to_Materials_Characterization__CHM_412_Collaborative_Text/Spectroscopy/Energy-Dispersive_X-ray_Spectroscopy_(EDS). Apr. 2019. (Visited on 07/30/2024).

[74] The International Union of Pure and Applied Chemistry (IUPAC). *IUPAC - Auger Effect (A00520)*. https://goldbook.iupac.org/terms/view/A00520. DOI: 10.1351/goldbook.A00520. (Visited on 06/11/2024).

[75] *Auger Effect - an Overview — ScienceDirect Topics*. https://www.sciencedirect.com/topics/physics-and-astronomy/auger-effect. (Visited on 07/10/2024).

[76] Johannes Bernardi. "Energy-Dispersive X-ray Spectroscopy". In: May 2021. ISBN: 978-0-7503-3059-6. DOI: 10.1088/978-0-7503-3059-6ch41.

[77] Motohiro Uo, Takahiro Wada, and Tomoko Sugiyama. "Applications of X-ray Fluorescence Analysis (XRF) to Dental and Medical Specimens". In: *Japanese Dental Science Review* (Jan. 2014). DOI: 10.1016/j.jdsr.2014.07.001.

[78] Raju Kumar. *Characterization of X-ray Anode and Absorption Edges*. Mar. 2018. DOI: 10.13140/RG.2.2.11708.74882.

[79] *EDX*. https://www.epfl.ch/research/facilities/cmi/equipment/metrology/oxford-instruments-edx/. (Visited on 07/30/2024).

[80] Wladick Hartmann et al. "Waveguide-Integrated Broadband Spectrometer Based on Tailored Disorder". In: *Advanced Optical Materials* 8.6 (2020), p. 1901602. ISSN: 2195-1071. DOI: 10.1002/adom.201901602. (Visited on 07/25/2024).

[81] H. Gehring et al. "Low-Loss Fiber-to-Chip Couplers with Ultrawide Optical Bandwidth". In: *APL Photonics* 4.1 (Jan. 2019), p. 010801. ISSN: 2378-0967. DOI: 10.1063/1.5064401. (Visited on 07/25/2024).

[82] Helge Gehring et al. “Broadband Out-of-Plane Coupling at Visible Wavelengths”. In: *Optics Letters* 44.20 (Oct. 2019), pp. 5089–5092. ISSN: 1539-4794. DOI: 10.1364/OL.44.005089. (Visited on 07/25/2024).

[83] *Quantum X Align: 3D Printer with Nanoprecision Alignment System*. https://www.nanoscribe.com/en/products/quantum-x-align/. (Visited on 07/25/2024).

[84] Dr Rüdiger Paschotta. *Pulse Pickers*. https://www.rp-photonics.com/pulse_pickers.html. (Visited on 06/21/2024).

[85] F. Lukiyanov, Rau Eduard, and R. Sennov. “Depth Range of Primary Electrons, Electron Beam Broadening, and Spatial Resolution in Electron-Beam Studies”. In: *Bulletin of the Russian Academy of Sciences: Physics* 73 (Apr. 2009), 441–449
. DOI: 10.3103/S1062873809040029.

[86] Chengyun Wang, Gong Liwen, and Zhao Guiwen. “Preparation of Er2O3 Thin Films by Sol-Gel Dipping Process”. In: *Journal of Materials Science: Materials in Electronics* 13 (Mar. 2002). DOI: 10.1023/A:1014389502190.

[87] William C. Moore. “AQUA REGIA: PRELIMINARY PAPER.” In: *Journal of the American Chemical Society* 33.7 (July 1911), pp. 1091–1099. ISSN: 0002-7863. DOI: 10.1021/ja02220a009\\. (Visited on 07/25/2024).

[88] “30 - The Lanthanide Elements (Z = 58–71)”. In: *Chemistry of the Elements (Second Edition)*. Ed. by N. N. Greenwood and A. Earnshaw. Oxford: Butterworth-Heinemann, Jan. 1997, pp. 1227–1249. ISBN: 978-0-7506-3365-9. DOI: 10.1016/B978-0-7506-3365-9.50036-5. (Visited on 07/25/2024).

[89] . *Brockhaus ABC Chemie*. Leipzig: Brockhaus Verlag, 1965.

[90] UCIRVINE. *RCA-1 Silicon Wafer Cleaning*.

[91] Ian McN Smallwood. *Handbook of Organic Solvent Properties*. Literaturverz. S. [305] - 306. New York: Halsted Pr. (Wiley), 1996. ISBN: 978-0-340-64578-9 978-0-470-23608-6.

[92] *Allresist_Product-information_Remover_AR-600-71_AR-300-70-72-73-76_English_web.Pdf*. https://www.allresist.com/wp-content/uploads/sites/2/2021/02/Allresist_Product-information_Remover_AR-600-71_AR-300-70-72-73-76_English_web.pdf. (Visited on 07/25/2024).

[93] J. Roger Hart. “Ethylenediaminetetraacetic Acid and Related Chelating Agents”. In: *Ullmann’s Encyclopedia of Industrial Chemistry*. Ed. by Wiley-VCH Verlag GmbH & Co. KGaA. Weinheim, Germany: Wiley-VCH Verlag GmbH & Co. KGaA, June 2000, a10_095. ISBN: 978-3-527-30673-2. DOI: 10.1002/14356007.a10_095. (Visited on 07/25/2024).

[94] Ian W. M. Smith. “The Temperature-Dependence of Elementary Reaction Rates: Beyond Arrhenius”. In: *Chem. Soc. Rev.* 37.4 (2008), pp. 812–826. ISSN: 0306-0012, 1460-4744. DOI: 10.1039/B704257B. (Visited on 07/25/2024).

[95] *ANDO AQ6330 Datasheet.Pdf*. https://accusrc.com/uploads/datasheets/ANDO%20AQ6330%20Datasheet.PDF. (Visited on 07/16/2024).

[96] *Mounted Achromatic Doublets, AR Coated: 400 - 1100 Nm*. https://www.thorlabs.com/newgrouppage9.cfm?objectgroup_id=12804&pn=AC254-075-AB-ML#12806. (Visited on 06/22/2024).

7 Appendix

Crystal structure	KNO_3:$Er(NO_3)_3$ weight [g:g]	Doping temperature [°C]	Doping time [hours]	Annealing temperature [h]	Annealing time [hours]	Cracked?
x-cut	27:0.2	465	4	200/300/400	8/8/23	yes
				450	23	no
		530	4	200/300/400	8/8/23	no
		600	4	200/300/400	8/8/23	no, but damaged
x-cut	27:0.3	465	4	200/300/400	8/8/23	no
		495	4	200/300/400	8/8/23	no, edges damaged
x-cut	27:0.4	465	4	200/300/400	8/8/23	no
		530	4	200/300/400	8/8/23	yes
		600	4	200/300/400	8/8/23	no, but damaged
x-cut	27:0.6	465	4	200/300/400	8/8/23	no
				465	23	no
		495	4	200/300/400	8/8/23	no
			4	450	23	no
				500	23	yes
				550	23	no
				600	23	yes
x-cut	27:0.8	465	4	200/300/400	8/8/23	no
		495	4	200/300/400	8/8/23	yes
x-cut	27:1.0	465	4	200/300/400	8/8/23	no, but damaged
		530	4	200/300/400	8/8/23	yes
		600	4	200/300/400	8/8/23	No, but damaged
x-cut	27:2.0	495	4	200/300/400	8/8/23	yes
x-cut	27:3.1	465	4	200/300/400	8/8/23	yes
x-cut	27:4	465	4	200/300/400	8/8/23	no, but damaged
		530	4	200/300/400	8/8/23	yes
		600	4	200/300/400	8/8/23	yes

Figure 31: Overview of x-cut chips and the applied parameters

Crystal structure	KNO_3:$Er(NO_3)_3$ weight [g:g]	Doping temperature [°C]	Doping time [hours]	Annealing temperature [h]	Annealing time [hours]	Cracked?
z-cut	27:0.2	465	4	200/300/400	8/8/23	yes
				450	23	no
		530	4	200/300/400	8/8/23	no
		600	4	200/300/400	8/8/23	no, but damaged
z-cut	27:0.3	465	4	200/300/400	8/8/23	no
		495	4	200/300/400	8/8/23	yes
z-cut	27:0.4	465	4	200/300/400	8/8/23	no, but damaged
		530	4	200/300/400	8/8/23	yes
		600	4	200/300/400	8/8/23	no, but damaged
z-cut	27:0.6	465	4	200/300/400	8/8/23	no, but damaged
				450	23	no
		495	4	200/300/400	8/8/23	no
z-cut, s-shape	27:0.6	465	4	450	23	no
z-cut	27:0.8	465	4	200/300/400	8/8/23	no
		495	4	200/300/400	8/8/23	no
z-cut	27:1.0	465	4	200/300/400	8/8/23	no, but damaged
		530	4	200/300/400	8/8/23	yes
		600	4	200/300/400	8/8/23	no, but damaged
z-cut	27:2.0	495	4	200/300/400	8/8/23	yes
z-cut	27:3.1	465	4	200/300/400	8/8/23	yes
z-cut	27:4	465	4	200/300/400	8/8/23	no, but damaged
		530	4	200/300/400	8/8/23	yes
		600	4	200/300/400	8/8/23	no, but damaged

Figure 32: Overview of z-cut chips and the applied parameters

Chemical compound	Concentration	Duration	Effect: dirt crystals	Effect: TFLN	Other effects & comments
DM Water (H_2O)	-	1 min*	no	no	no
		5 min*	no	no	no
		1 min* + 1min in sonicator*	>99% removed	no/minor damage	all Er removed
		1 min* + 30 s in sonicator*	>99% removed	no/minor damage	all Er removed
		1 min* + 10 s in sonicator*	>99% removed	no/minor damage	all Er removed
		1 min* + 2 s in sonicator*	>60% removed	no/minor damage	all Er removed
		5 min in sonicator*	>99% removed	no/minor damage	all Er removed
		14 h gradually heating to 250°C**	little removing	no/minor damage	new Na, Ca & Mg crystals
		10 h gradually heating and 6 h cooking a 100°C **	little removing	minor damage	Na, Ca & Mg crystals removed again
		15 h	no	no	K fully removed
		43 h + 50°C heat	no	no	even K not fully removed
Sodium thiosulfate ($Na_2S_2O_3$)	< 0.1 M	30 s	no	no	no
	0.1 M	21 h	no	minor damage	no
		66 h	only pepples left	minor damage	no
		66 h + 30s HCL	pepples still left	minor damage	no
Sulfuric acid (H_2SO_4)	95%-97%	2 min	no	no	no
		25 h	fully removed	plate-like shifted	new Al-, Na- & K-crystals
Hydrochlorid acid (HCL)	≥ 37%	30 s	no	minor damage	no
		2 min* + 1 min acetid before*	medium removing	little damage	no Er in TFLN
		5 h	little removing	minor damage	no
		21 h	fully removed	minor damage	no Er in TFLN
Phosphoric acid (H_3PO_4)	85%	30 s	no	no	no
		2 min	fully removed	no	no Er in TFLN

Figure 33: Overview of all applied cleaning attemps part 1

Ethylenediaminetetra-acetic acid (EDTA)	0.1 M	21 h	no	minor damage	no
		66 h	no	minor damage	no
Acetid acid ($C_2H_4O_2$)	100%	1 min*	medium removing	little damage	no Er in TFLN
		4 h + 50°C heat	no	no	no (for x- and z-cut, increased amount of acid)
		21 h	medium removing	no	no
		23 h + 50°c heat	little/ medium removing	no	no Er in z-cut TFLN (in x-cut: Er existing)
		25 h	medium cleaned	completely damaged	no (increased amount of acid)
		66 h	medium removing	no	1/3 of Chips no Er in TFLN
		64 h	no	no	same dirt
Citric acid ($C_6H_8O_7$)	1 M	3 min *	little removing	little damage	no Er in TFLN
		21 h	no	medium damaged	no
		21 h + 50°c heat	medium/good removing	no	no Er in TFLN
		66 h	bigger pepples left	½ chips no damage ½ chips TFLN remove	no
		66 h + 30s HCL	pepples still left	minor damage	no
	2 M	64 h	almost removed	minor	almost all waveguides dirt-free
Aqua regia (HNO_3 + 3HCL)	1:3	1 min	almost removed	completely destroyed	no
RCA 1 (HCL + H_2O_2 + 5 H_2O)	1:1:5	1 min	little removing	minor damage	no
AR 60071 (7 $C_3H_6O_2$ + 3 $C_4H_{10}O_2$)	1:3	25 min	no	medium damage	no

M = mol/l

*** = the cleaning took place immediately after the doping before the annealing process**

**** = the dirt crystals are cooked out of the chip by doing the annealing inside a water bath**

Figure 34: Overview of all applied cleaning attemps part 2